Hindawi
Structural Control and Health Monitoring
Volume 2023, Article ID 3647434, 26 pages
https://doi.org/10.1155/2023/3647434

Research Article

Rapid Three-Dimensional Reconstruction of Underwater Defective Pile Based on Two-Dimensional Images Obtained Using Mechanically Scanned Imaging Sonar

Sheng Shen,[1] **Yamian Zeng**,[2] **Changqin Lai**,[1] **Shaofei Jiang**,[1] **Shaofen Wu**,[3] **and Shenglan Ma**[4]

[1]*College of Civil Engineering, Fuzhou University, Fuzhou 350108, China*
[2]*College of Civil Engineering, Quanzhou University of Information Engineering, Quanzhou 362008, China*
[3]*Fujian Expressway Science & Technology Innovation Research Institute Co. Ltd., Fuzhou 350013, China*
[4]*Fujian Provincial Key Laboratory of Advanced Technology and Informatization in Civil Engineering, Fujian University of Technology, Fuzhou 350118, China*

Correspondence should be addressed to Sheng Shen; s_shen@126.com and Shaofei Jiang; cejsf@fzu.edu.cn

Received 18 October 2022; Revised 4 February 2023; Accepted 3 March 2023; Published 28 March 2023

Academic Editor: Ka-Veng Yuen

Three-dimensional (3-D) reconstruction based on sonar imaging is an intuitive and comprehensible form for describing an underwater defective pile. Most existing 3-D reconstruction methods are inefficient as they require the extraction of numerous feature points from many sonar images. A rapid 3-D reconstruction method for underwater defective piles based on two-dimensional (2-D) images obtained using mechanically scanned imaging sonar (MSIS) is proposed herein. First, the correspondences between the geometric features of MSIS images and actual defects are established based on the mapping relationship between actual object and MSIS image. Subsequently, no more than three feature points are extracted from 2-D MSIS images to recognize the contour segments. The contour segments are assembled into the entire cross section and then into the entire defective pile. The applicability of the proposed method is verified via a 3-D reconstruction for a scaled-down pile with multiple defect distributions.

1. Introduction

Concrete piles embedded completely in a riverbed are essential load-bearing members in cross-river and cross-sea bridges. During the long-term service period of these bridges, riverbed scour can partially expose the piles (Figure 1(a)), thus resulting in a case similar to an elevated pile-cap foundation, as shown in Figure 1(b). The shielding of these exposed piles may degrade, crack, and break gradually owing to the effect and immersion of flowing water; thus, regular underwater inspections must be performed to reduce potential risks that can degrade the structural stability and safety of the entire bridge. In cases involving clear water, optical-based visual inspection by trained divers is typically conducted to efficiently provide an accurate and realistic description of defects on the pile surface [1–3]. However, high turbidity caused by bubbles, floating debris, and other objects can degrade the clarity of the obtained optical images and distort the details of defects significantly, even when physics-based image enhancement techniques are applied [4–6]. By contrast, sound signals can penetrate mud, bubbles, and various other floating objects and then proceed to propagate deeper. Therefore, various sonar imaging systems have been proposed and applied for inspecting cracks in dams [7], monitoring scour [8–14], and detecting surface defects in underwater piles [15–17] and piers [18, 19].

The defect detection of underwater concrete piles involves target detection [20–22], tracking [23], and sonar positioning [24]. Although a series of algorithms based on

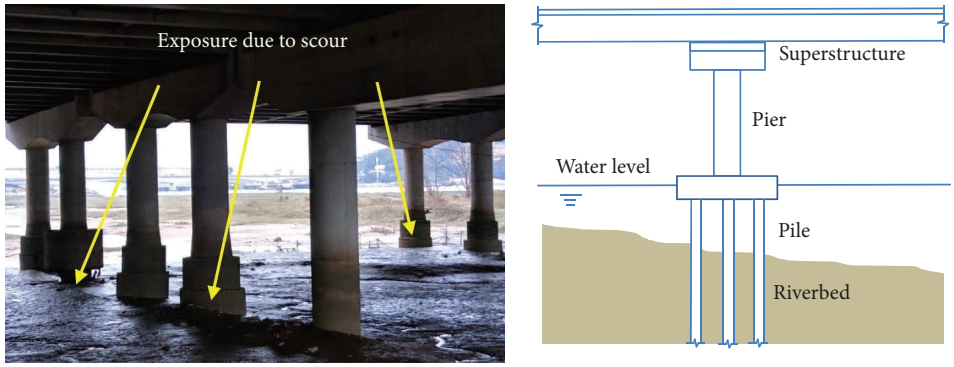

Figure 1: Actual photo and sketch of exposed piles. (a) Partial exposed piles caused by scour. (b) Elevated pile-cap foundation.

artificial neural networks [20], deep learning [21, 22], and numerical filters [23] has been proposed and successfully applied to detect divers, shoals of fish, autonomous underwater vehicles, and their movements at sea, these methods cannot be directly applied for detecting defects in underwater concrete piles, owing to the difference in the detection purpose and the operating environment. In most proposed algorithms, the suspected object is typically directly recognized as the target even with the presence of significant background noise, provided that the suspected object in the sonar image conforms approximately to the shape of the target. By contrast, because sonar is typically near a pile, the signal-to-noise ratio of the image obtained is generally high, and the characteristics of defects are shown clearly. However, owing to the difference in the relative distance, relative orientation, and relative attitude between the defect and sonar, a defect can exhibit distinct characteristics in different sonar images. Thus, the relationship between each defect and its corresponding image characteristics must be established under different conditions based on the imaging principles of sonar, and the defect size must be measured accurately. In summary, existing methods primarily focus on the target positioning rather than its sizes, and an accurate shape of the defect is significant for detecting defects in piles.

Unlike optical images, sonar images are more difficult to interpret and understand intuitively because of the difference between the principles of optical and acoustic imaging. Therefore, to show the detailed sizes of defects on defective piles, a 3-D model reconstruction based on sonar imaging was developed using two methods. The first method uses 3-D imaging sonar, such as Bv5000 [17] (produced by Teledyne Marine) and Aris1800 [25] (produced by Sound Metrics), to measure the 3-D sizes of the defects. Although this method appears to be simple to operators, it presents two significant disadvantages in terms of data accuracy. Most 3-D imaging sonars can barely detect small defects in the concrete cover of a pile owing to their insufficient measurement sensitivity and precision. The results of a laboratory test [17] indicated that for a distance of 5 m between the sonar and pile, the measurement errors of the length, width, and depth of a cavity in the pile surface could reach 2 cm. The minimum resolution was at least 5 cm, which is similar to the typical cover thickness of a concrete pile. In practical scanning, sonar is often placed approximately tens of meters away from piles to avoid potential collisions [10, 11], which is much further than that implemented in the aforementioned laboratory test. This distance of tens of meters may further compromise the capability of 3-D sonar in distinguishing defects measuring several centimeters during scanning. The quality of acoustic images depends on the stability of the sonar during imaging. However, the obtained images are often blurry because of the difficulty of the sonar-carrying boat in maintaining stationarity in strong currents with a velocity exceeding 4 knots [26]. In addition, the low scanning speed of several minutes to tens of minutes for large-angle scanning of 3-D sonar increases the difficulty in maintaining the stability of the sonar for a long duration under the effect of water flow. Therefore, the existing civil 3-D imaging sonars cannot satisfy the requirements of clarity and accuracy in the defect detection of underwater concrete piles.

Another method is to replace 3-D imaging sonar with two-dimensional (2-D) imaging sonar with a higher scanning speed, followed by reconstructing the 3-D model by assembling the 2-D images obtained by scanning an object from various directions. This method is challenging in terms of contour feature extraction from 2-D images, followed by pattern classification. First, 2-D imaging sonar can only measure the size of a defect in two directions. The echo-intensity-based interpretation of object size in the third direction of a 2-D sonar image can be complicated because of the interference of backscatter signals from multiple reflective surfaces in one wave beam. In addition, the contour of the signal-interfered region varies with the relative positions of the sonar and defect. Establishing a one-to-one correspondence between the physical defect and the corresponding 2-D sonar image is thus challenging. Hence, correspondence analysis is rarely reported.

Combining a shape via shading [27] and 2-D maps (a depth map and an intensity map) [28] based on a side-scan sonar can provide insights for reconstructing a 3-D model of the seabed surface and underwater objects. However, the shape obtained from shading cannot provide satisfactory

precision during the 3-D reconstruction [29]. Synthetic aperture sonar has been proposed for reconstructing a 3-D model by scanning an object from multiple positions around it [30]. However, expensive navigation sensors are required to accurately navigate synthetic aperture sonars. Recently, a method of carving geometric spaces using images obtained from forward-looking sonar has been proven to be feasible for 3-D reconstruction [31, 32]. Based on multiple 2-D acoustic images from specified scan positions around the target as well as the poses of the forward-scan sonar, the unoccupied 3-D space in the projected image sequence of the target was sequentially eliminated, and the remaining volume of space was the estimated volumetric model of the target. The accuracy of the reconstructed contour of an object depends on the number of target-projected images in multiple directions. For example, the volumetric error percentages of concave reconstructions using 64 sonar images can reach 40%, and the error percentages of wood table reconstructions using 32 images can reach 60% [32]. In practice, performing scans around a single pile multiple times is uneconomical and reflects low detection efficiency. Nonetheless, insufficient images may result in significant errors if the geometric space-carving method is applied directly.

To avoid these difficulties, we herein propose an alternative 3-D model reconstruction strategy for a defective pile based on only six to eight 2-D MSIS images obtained at a few scan points along a circular path around the pile. First, the correspondence between the physical defects on the pile surface and the sonar images is ascertained. Subsequently, the feature points of the defect contour are extracted from the obtained sonar images. Finally, the estimated 3-D model is constructed using the horizontal contours of the pile section formed by connecting these feature points smoothly.

This paper is organized as follows. Section 2 introduces the 2-D imaging principles of a mechanically scanned imaging sonar (MSIS). Section 3 describes cavity and spalling, which are the two most typical forms of defects in imaging and are selected as the targets to be identified and reconstructed in this study; additionally, the features of the cavity and spalling in an MSIS image are discussed. When the defects are completely within an MSIS image, Sections 4 and 5 describe the one-to-one quantitative correspondence among the cavity, spalling, and their image features in cases involving various relative positions between the sonar and defects. Sections 6 proposes how to determine the contour of the defect when the defect spans two successive images and shows a 3-D reconstruction process for these defects based on the sequence of MSIS images. The applicability of the proposed 3-D model rebuilding method is experimentally verified in Section 7 based on a reconstructed 3-D model for a scaled-down pile with multiple defects.

2. Imaging Principle of MSIS and Mapping between Actual Pile and MSIS Image

2.1. Introduction of MSIS. An MSIS is a type of active imaging sonar widely used to detect underwater targets as well as to measure and pictorially display their range, direction, and size. Compared with other types of imaging sonar, such as forward-looking and side-scan sonars, an MSIS is disadvantageous as it does not allow moving objects to be scanned. However, an MSIS may be the best option for pile scanning owing to two reasons. First, the underwater pile is immobile, which implies that the MSIS can easily acquire the acoustic images of the pile surface. In addition, the orientations of the transducers of forward-looking and side-scan sonars are typically fixed. Thus, the scan fields of both types of sonar are relatively narrow and limited, although their scanning and imaging speeds are high. By contrast, an MSIS features a transducer suspended below water that can rotate 360° on a fixed base to transmit and receive sound waves. It requires only dozens of seconds to completely scan a vertical strip on the pile surface and can improve the scanning efficiency for long piles. A comparison of the scan field of the MSIS and other types of imaging sonars is shown in Figures 2(a) and 2(b).

Sonars can only detect objects in their respective scan fields. The scan field of an MSIS is determined by the horizontal beamwidth, sector width, and scan range, whereas the scan precision primarily depends on the vertical beamwidth and step size. As shown in Figure 3(a), the transducer emits a pulse in water with a fixed horizontal beamwidth and vertical beamwidth. Subsequently, the signal reflected from the surface of an object with a distance less than the scan range is received and recorded by the transducer. The transducer rotates by a small angle, which is known as the step size, and repeats the signal transmission and reception. When the rotation of the transducer reaches the predesigned sector width, a pseudo-color acoustic image of the scanned object can be generated from the accumulation of the signal received. The color difference between the different areas of the image represents the intensity of the reflected signal, which is primarily related to the shape and properties of the object surface.

However, the MSIS cannot distinguish between two objects located on the same wave beam that are at the same distance from the transducer. As shown in Figure 3(b), the transducer receives two echoes from Objects 1 and 2 simultaneously because they are located on the same signal arc. In this case, the MSIS can only indicate the presence of an object at a certain distance but cannot differentiate between Objects 1 and 2. Therefore, the horizontal beamwidth should be decreased to increase the resolution.

2.2. Mapping between the Real Objects and the MSIS Images. Although the field of view of an MSIS is a 3-D sector space, the MSIS can only obtain a 2-D image by projecting the 3-D sector space to a plane; consequently, the information in the direction perpendicular to the projection plane is concealed. To restore the concealed information, the actual 3-D objects of various shapes must be mapped to the corresponding 2-D MSIS images.

The echoes received by the MSIS can form a circular or sector-shaped acoustic image that corresponds to the target area within a range of 360° or a prespecified angle. Figure 4(a) shows a polar coordinate system that appoints the

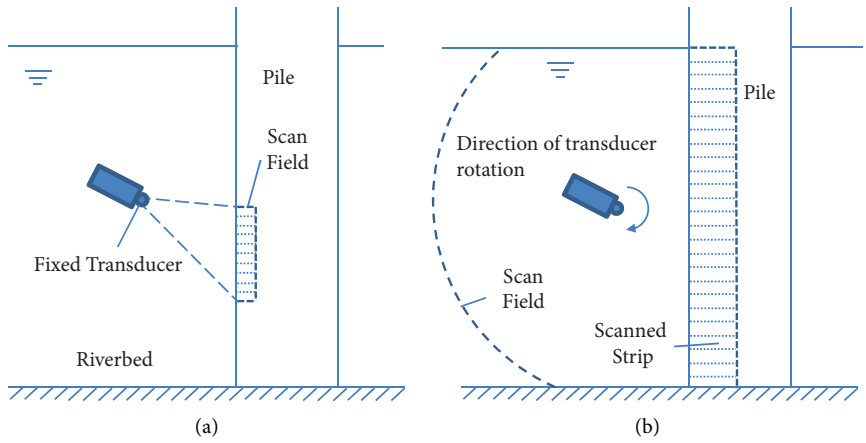

Figure 2: Comparison of the scan fields on a pile by different sonars. (a) Scan field on a pile by other sonars. (b) Scan field on a pile by an MSIS.

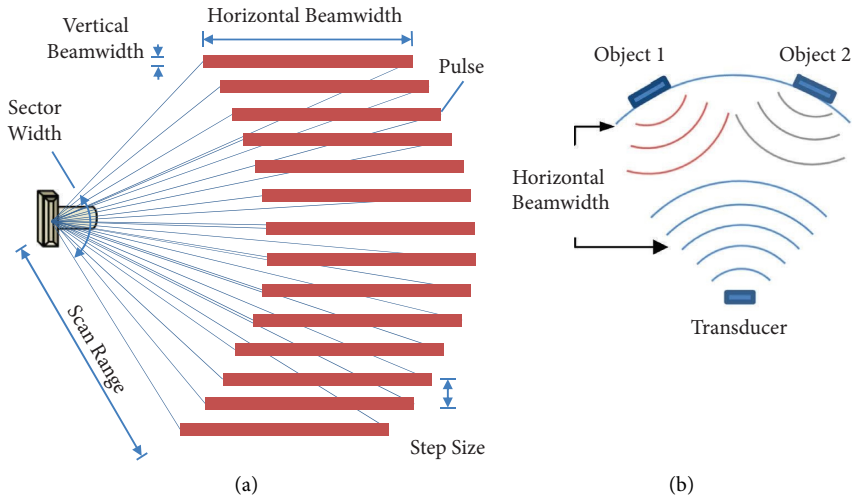

Figure 3: Some basic concepts of pulse emission and reflection of the MSIS. (a) The scan field of the MSIS. (b) Two signal reflections in the same beamwidth.

location of the transducer of the MSIS as the original point (point O) in an acoustic image. A 3-D Cartesian coordinate system, as illustrated in Figure 4(b), is established with point O as its original point and the Z-axis as the rotation axis of the transducer. The transducer emits a wave beam rotating around the Z-axis with a horizontal beam width of α and a scanning range of D.

Figures 4(a), 4(c), and 4(e) show three acoustic images corresponding to the actual scenes presented in Figures 4(b), 4(d), and 4(f), respectively. Point M at the coordinates (ρ, ω) in Figure 4(a) corresponds to the space arc $M'M''$ in Figure 4(b), where the coordinates of M'', M, and M' are $(\rho, \omega, -\rho\sin(\alpha/2))$, $(\rho, \omega, 0)$, and $(\rho, \omega, \rho\sin(\alpha/2))$, respectively [33, 34]. This implies that if an object at any point $M'M''$ in Figure 4(b) generates an echo, then the color of point M in Figure 4(a) will change to bright yellow. By contrast, point M remains black if no echo is generated on the arc. Moreover, the straight line AB in Figure 4(c) corresponds to the spatial curved surface $A''A'B'B''$ in Figure 4(d). Both the line in Figure 4(c) and the spatially curved surface in Figure 4(d) are symmetric and vertical to the Y-axis. Furthermore, the planar trapezium ABCD in Figure 4(e) corresponds to the space body $A''A'B'B''D''D'C'C''$ in Figure 4(f). Both the planar trapezium and space body are symmetric and vertical to the Y-axis.

Figure 5 shows an example of an intact pile and a defective pile mapped to the corresponding MSIS images. Figures 5(a) and 5(b) show a pile with a cavity and the scanning location of an MSIS. Figures 5(c) and 5(d) give the MSIS image of an intact pile and the pile with a cavity. Figures 5(e) and 5(f) illustrate the analysis of the corresponding mapping relationship. Based on the imaging principles of the MSIS, the region occupied by beams in Figures 5(c) and 5(d) appears as a yellow vertical strip of a certain width, and the uncovered region remained black. The left edge of the yellow strip indicates the edge closest to the sonar in the beam-occupied area on the pile, and the right edge of the bright strip represents the boundary

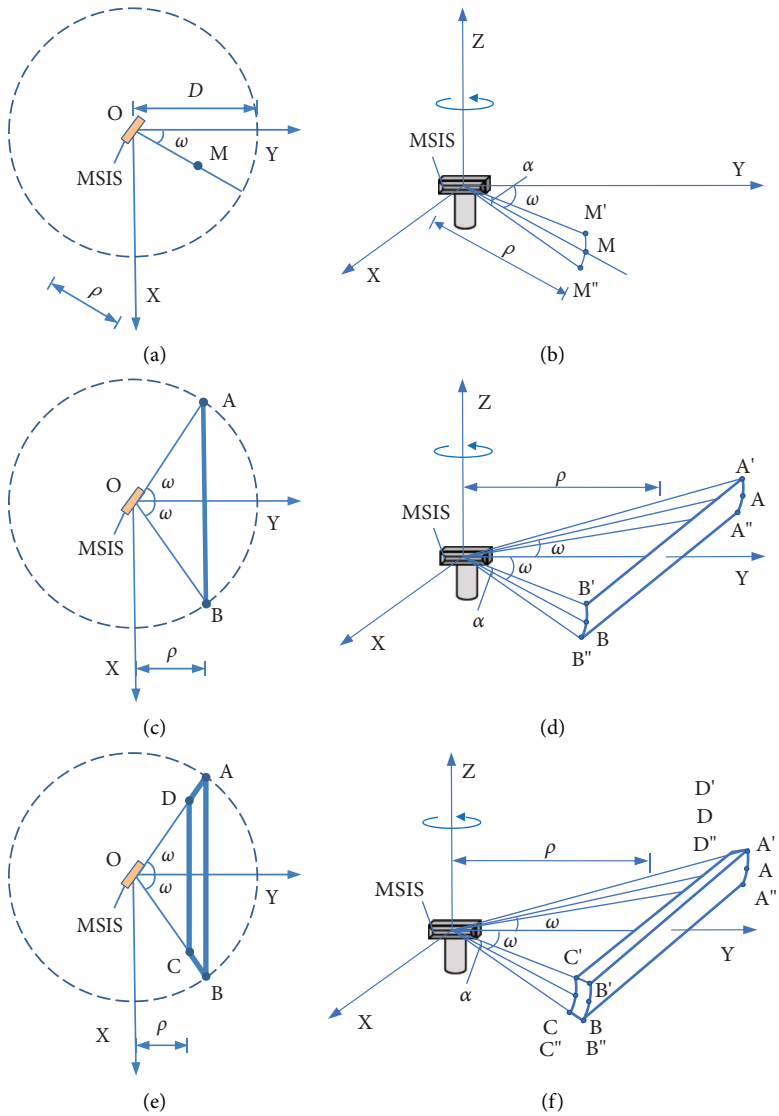

FIGURE 4: The mapping between the 2-D MSIS images and the 3-D real scene. (a) A point in the 2-D polar coordinate system. (b) A space arc in the 3-D Cartesian coordinate system. (c) A line in the 2-D polar coordinate system. (d) A spatial curved surface in the 3-D Cartesian coordinate system. (e) A planar trapezium in the 2-D polar coordinate system. (f) A space body in the 3-D Cartesian coordinate system.

between the beam-occupied and unoccupied areas. In Figure 5(e), the actual distance from point M on the pile surface to the sonar transducer is denoted by a', as illustrated in Section 1-1, and the projected distance a from the side view is shorter than a'. However, the distance a'' shown in the 2-D MSIS image equals a' rather than a. This implies that although the 2-D MSIS image of an intact pile is similar to the optical side view of the same pile, both images differ in terms of the distance measurement owing to the difference between the principles of optical and acoustic imaging. Figure 5(b) shows the defective pile with a cavity mapped to the corresponding MSIS image. Although points M and N are located on the same horizontal line, the former is located on the edge of the cavity, whereas the latter is located on the projection plane. Here, a, a', a'' and b, b', b'' are the projected distances in the side view, the actual distances, and the distances detected by the MSIS, respectively. Because N is on the projection plane but M is not, $a' = a'' > a$ and $b' = b'' = b$. Based on Figures 5(e) and 5(f), all the horizontal coordinates of an object in an optical image are different from those in the corresponding acoustic image, except for the points located on the projection plane. However, all the vertical coordinates in the two images are equal. Furthermore, the cavity shown in the MSIS image is brighter than the surrounding straight strip because the concave surface of the cavity provides stronger reflection than the convex surface of the intact pile.

3. Two Types of Typical Defects on Underwater Piles

3.1. Primary Types of Defects on Underwater Piles. According to the Chinese standard [35], several types of defects exist in long-term-served underwater piles, such as

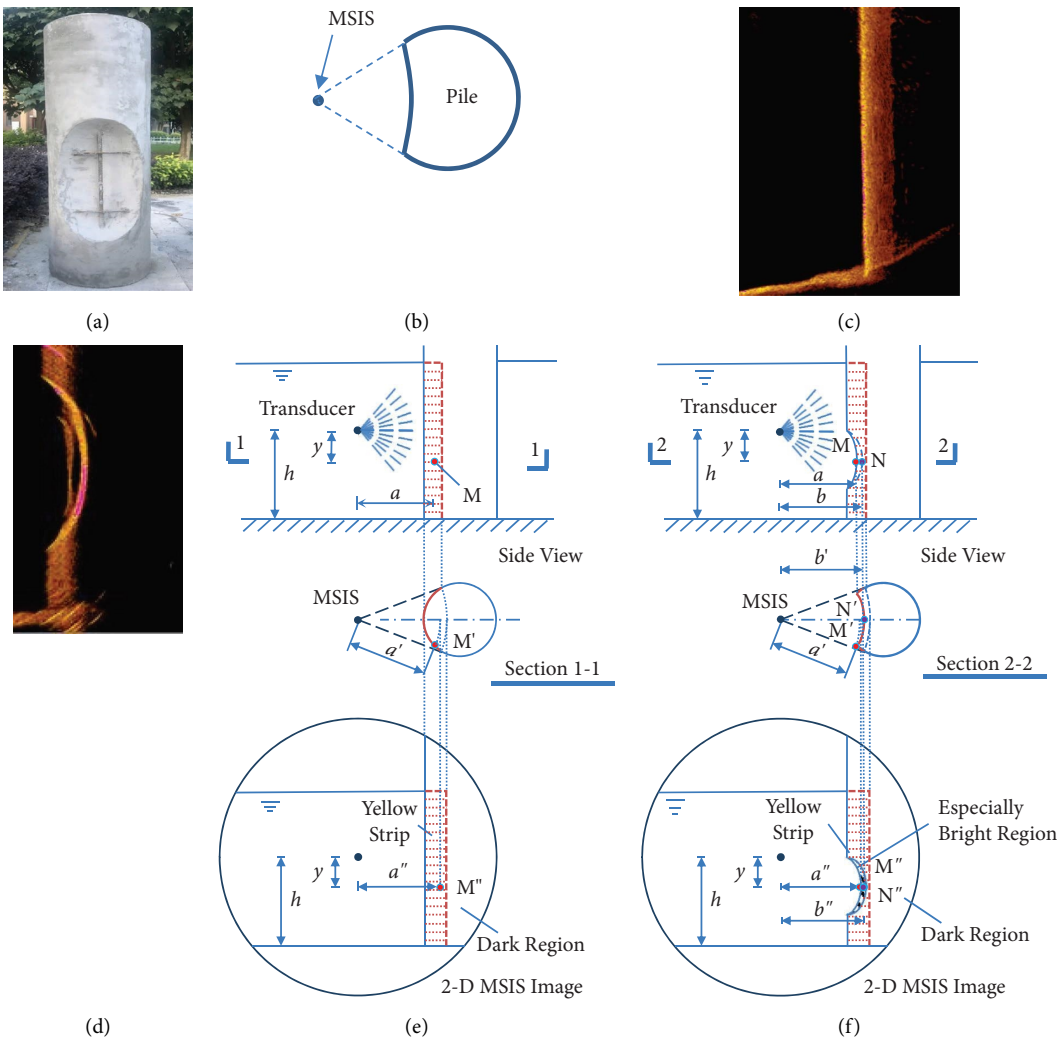

Figure 5: The mapping between the real piles and the corresponding MSIS images. (a) The defective pile. (b) Sonar and pile. (c) MSIS image of an intact pile. (d) MSIS image of the defective pile. (e) Mapping of sonar image and intact pile. (f) Mapping of sonar image and defective pile.

voids, abrasion, cracks, cavities, spalling, and material corrosion. However, most forms of chemical corrosion, other than physical damage, are barely detected by acoustic or optical scanning. Minor defects, including voids, hungry spots, abrasion, and cracks with widths of less than 5 mm owing to slight variations in the surface, are often overlooked. Therefore, the defects that can be detected and repaired using the method proposed herein are primarily cavities and spalling on the surface of underwater defective piles.

3.2. Features of Cavity and Spalling in MSIS Image. A cavity refers to a hole with a depth that approaches or exceeds the thickness of the concrete cover of the pile. Spalling refers to the phenomenon of concrete collapsing from the surface when coarse aggregates are exposed. Figures 6(a) and 6(b) present two typical cases of cavity and spalling, respectively [34], whereas Figures 6(c)–6(e) show the corresponding MSIS images of the intact pile, cavity, and spalling, respectively. Each pile in Figures 6(c)–6(e) features a yellow strip of different widths with clear edges on both sides. The region in Figure 6(d), which corresponds to the cavity, shows an arc edge similar to the inner surface of the cavity, as shown in Figure 6(a). The spalling shown in Figure 6(e) features an approximately linear outline resembling spalling on the surface of an underwater pile, as shown in Figure 6(b). These features facilitate significantly in determining the location and type of defects on the pile surface.

3.3. Presumptions Applied to Simplify Reconstruction. In practical reconstruction, various feasible reconstructed defect contours exist owing to the limited known images. For example, in an actual inspection, no more than six to eight scanning points are typically placed around a pile to ensure the desired inspection speed, which implies that a single defect can be scanned and imaged to only one or two adjacent sonar photos. This indicates that the geometric space-carving method based on tens of sonar images is unsuitable

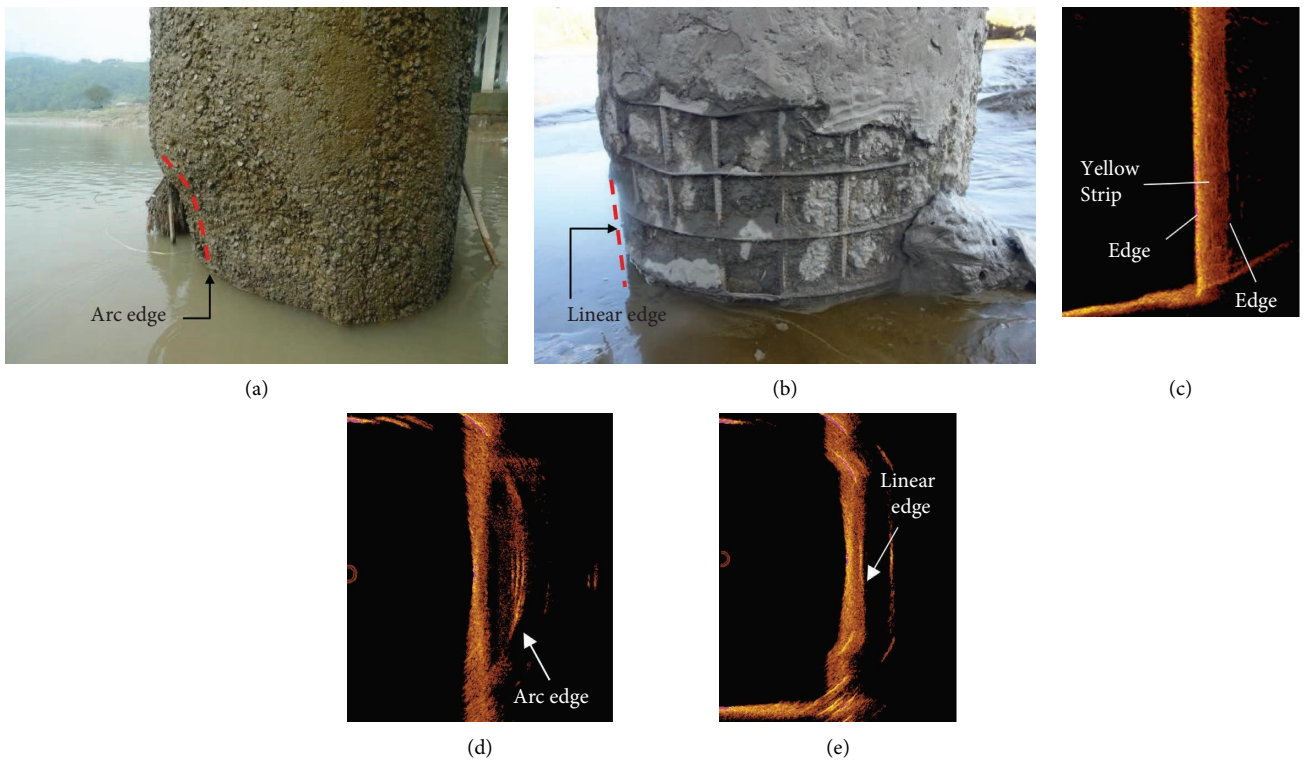

Figure 6: Photos and MSIS images of a cavity and a spalling on a pile surface. (a) A typical case of cavity [36]. (b) A typical case of spalling [36]. (c) An intact pile. (d) Cavity. (e) Spalling.

for the 3-D model reconstruction of defective piles. Therefore, the following presumptions are applied to remove any redundant possibilities caused by insufficient known conditions.

Presumption I: Because long-term scour by water flow can smooth the most significant convex and concave areas on the surface, the contour of each horizontal section of a cavity or spalling is decomposed reasonably into several smooth curves, including circular arcs with different radii. Thus, the coordinates of only three points must be ascertained from the sonar image before determining the expression for each circular arc.

Presumption II: If the redundant feasibility of the defect contour remains difficult to eliminate via analysis using multiple images obtained at several scanning points, then the identified contour corresponding to the worst damage is regarded as the contour that is the most similar to the actual defect contour. Thus, the consequences of the defect should not be underestimated in subsequent safety assessments.

4. Contour Recognition of Cavity Section Based on Single MSIS Image

The variation in the relative positions between the MSIS and defects or the varying distinct inner surface of the defect may result in MSIS images with significantly different geometric features. Although the preestimation of the relative positions and defect shapes is arduous, all the MSIS images of cavity can be classified into four types for cavity contour recognition. Moreover, prior to contour recognition, typical image processing methods, including denoising, edge enhancement, and histogram equalization, are applied to the raw MSIS images to obtain clear features.

4.1. Type I Image. Type I image of the cavity obtained from the MSIS is illustrated in Figure 7(a). The area covered by oblique lines is the partial surface of the pile covered by a sound wave. The sonar is placed at O_s. The signal-occupied region is uniformly segmented into n zones. The middle section of the ith zone is referred to as Section i, and i ranges from 0 to $n-1$. Meanwhile, h_i represents the vertical distance from Section i to O_s, where d is the horizontal distance from O_s to the pile edge. L_i and l_i represent the projected protrusion of the inner contour and the projected concavity for the outer contour of the cavity, respectively, where w is the projected width of the signal-occupied area.

A top view of Section i is shown in Figure 7(b), where O_p represents the center of the pile. The circular arc $A_3C_3B_3$ is drawn with O_s as the circle center and a radius of $d+w+L_i$, where A_3 and B_3 represent the two endpoints of the signal-occupied region, and C_3 is the intersection of $A_3C_3B_3$ and the straight line O_pO_s. The circular arc $A_1C_1B_1$ with a radius of $d+l_i$ is drawn similarly, where A_1, C_1, and B_1 represent the intersections of $A_1C_1B_1$ and straight lines O_sA_3, O_sO_p, and O_sB_3, respectively. D_1 and E_1 are the intersections of $A_1C_1B_1$ and the pile contour, respectively. A circular arc $A_2C_2B_2$ with

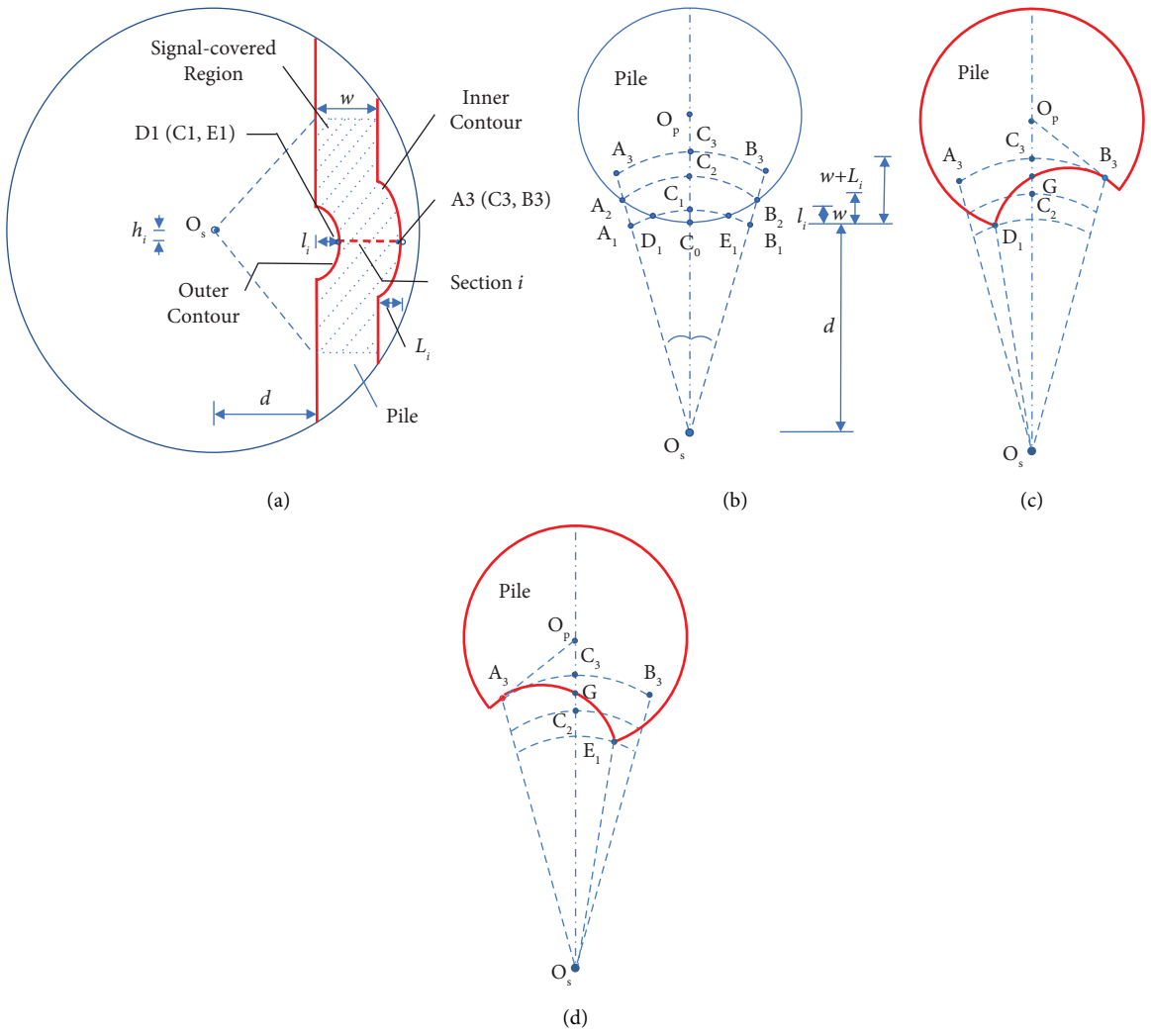

FIGURE 7: Two feasible cavity contours corresponding to Type I image. (a) Type I image. (b) Top view of Section *i*. (c) The 1st feasibility. (d) The 2nd feasibility.

a radius of $d+w$ is presented as well, where A_2, C_2, and B_2 represent the intersections of $A_2C_2B_2$ and O_sA_3, O_sO_p, and O_sB_3, respectively. A_2 and B_2 are the endpoints yielded by intersecting the signal-occupied region and the pile surface.

The geometric features of the signal-occupied region shown in Figure 7(a) can be expressed as $0 \le l_i < w$ and $L_i > 0$, which are used to estimate the contour of Section *i* shown in Figure 7(b). Based on the imaging principle of an MSIS, as explained in Section 2, an echoless point in an MSIS image indicates that the corresponding region in the 3-D space does not contain any echo. Thus, the cavity in Section *i* is placed between $D_1C_1E_1$ and $A_3C_3B_3$, as shown in Figure 7(b). Based on Presumption II in Section 3.3, D_1 and B_3 or E_1 and A_3 are placed reasonably on Section *i* of the cavity surface. Subsequently, an additional point G, which represents the midpoint of line segment C_2C_3, is appointed as the third point on the surface of the cavity. Thus, the symmetrical arcs D_1GB_3 and A_3GE_1, which are regarded as the cavity contour, are determined based on the known coordinates of D_1, G, B_3, A_3, and E_1.

4.2. Type II Image. The geometric features of the cavity shown in the Type II image (Figure 8(a)) can be described as $0 \le l_i < w$ and $L_i = 0$, which indicates that the contour of the cavity is located between circular arcs $D_1C_1E_1$ and $A_2C_2B_2$ in Figure 8(b). The positions of these points are the same as those of the corresponding points shown in Figure 8(b).

Three feasible contours of the cavity are shown in Figures 8(c)–8(e). Figure 8(c) shows a feasible cavity contour with minimum damage, whereas Figures 8(d) and 8(e) show the other feasible cavity contours, which are symmetrical to each other in shape. In Figure 8(c), circular arc $D_1C_1E_1$ is expressed based on the coordinates of points D_1, C_1, and E_1. In Figures 8(d) and 8(e), an additional point F, which is the midpoint of line segment C_1C_2, is designated as the third

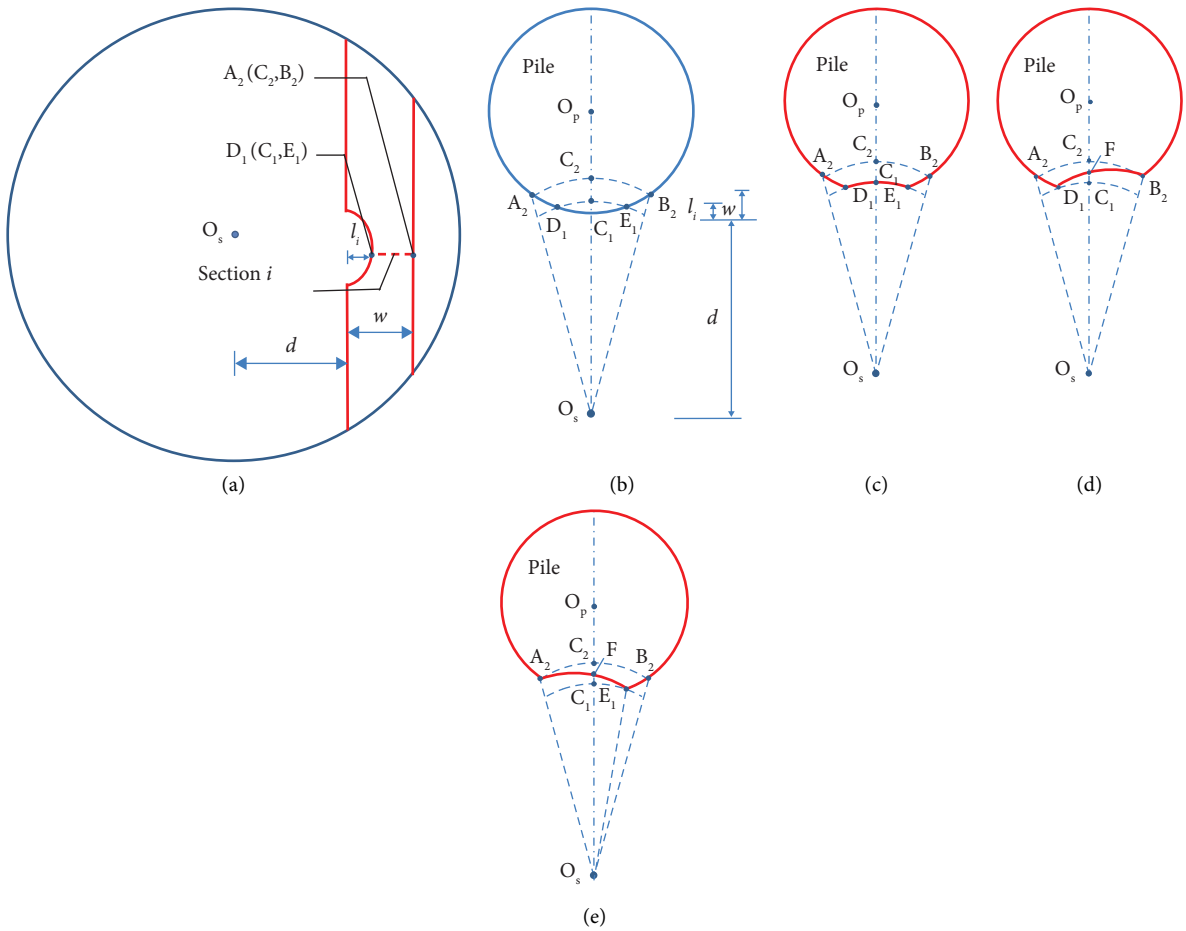

FIGURE 8: Three feasible cavity contours corresponding to Type II image. (a) Type II image. (b) Top view of Section *i*. (c) The 1st feasibility. (d) The 2nd feasibility. (e) The 3rd feasibility.

point on the cavity contour. Subsequently, arc D_1FB_2 or E_1FA_2 is determined.

4.3. Type III Image. In Figure 9(a), the geometric characteristics of the cavity image are described as $0 \le w < l_i$ and $L_i > l_i - w$, which indicates that the inner contour of the cavity in Section *i* is located between arcs $A_1C_1B_1$ and $A_3C_3B_3$ in Figure 9(b). The positions of these points are the same as those of the corresponding points shown in Figure 8(b).

The three types of feasible cavity contours are shown in Figures 9(c)–9(e). In Figures 9(d) and 99(e), an additional point *H*, which indicates the midpoint of line segment C_1C_3, is assigned as the third point on the surface of the cavity. Thus, arcs A_1HB_3 and A_3HB_1, as the cavity contours, are derived based on the coordinates of A_1, H, B_3, A_3, and B_1.

4.4. Type IV Image. The geometric characteristics of the cavity shown in Figure 10(a) are described as $l_i = 0$ and $L_i > 0$. In Figure 10(b), C_0 is the intersection of the pile and the line O_sO_p, and $l_i = 0$ indicates that a small area around C_0 is undamaged. Thus, damage can be assumed to occur entirely on either side of O_pC_0, while the surface on the other side is intact.

Figures 10(c) and 10(d) show two feasible contours of the cavity, respectively. Because only the coordinates of the two points in arcs C_0B_3 and C_0A_3 are known, two additional points *J* and *K*, which are the midpoints of line segments C_2B_3 and C_2A_3, respectively, are allocated on the surface of the cavity. Thus, arcs C_0JB_3 and C_0KA_3 for approximating the cavity contour can be determined based on three known coordinate points.

5. Contour Recognition of Spalling Section Based on Single MSIS Image

Similar to the explanation in Section 4, only two types of MSIS images correspond to the different relative positions of the sonar and pile and the different spalling shapes.

5.1. Type I Image. Figure 11(a) shows the geometric features of spalling as $0 \le l_i < w$ and $L_i > 0$, which implies that the spalling contour comprises at least one point on arc $D_1C_1E_1$ and another on $A_3C_3B_3$ (see Figure 11(b)). Figures 11(c)–11(e) illustrate all the three feasible spalling contours. In Figure 11(c), the contour of arc $A_3C_1B_3$ is determined by points A_3, C_1, and B_3, whose coordinates are known. However, in Figures 11(d) and 11(e), at least one additional

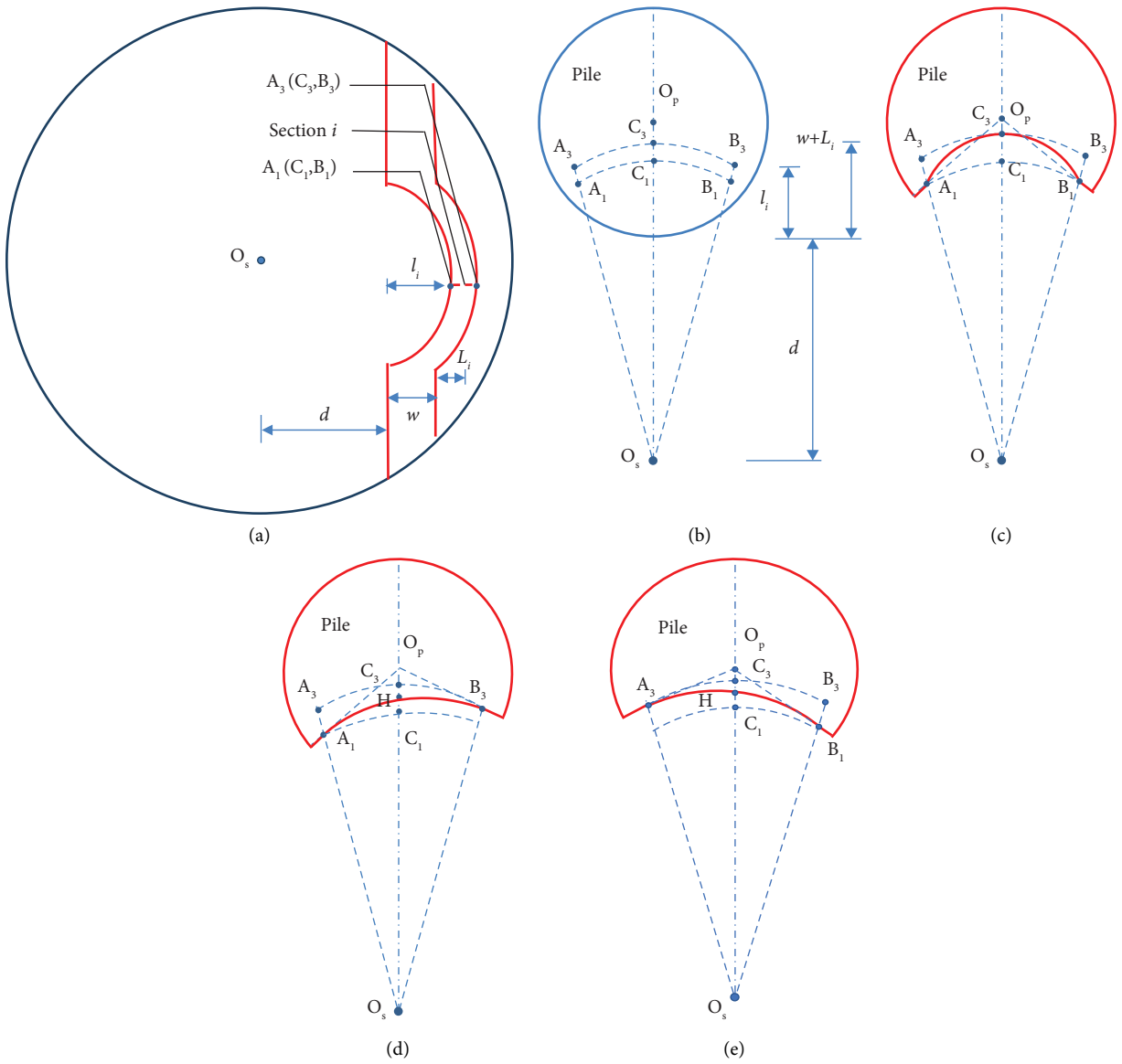

FIGURE 9: Three feasible cavity contours corresponding to Type III image. (a) Type III image. (b) Top view of Section *i*. (c) The 1st feasibility. (d) The 2nd feasibility. (e) The 3rd feasibility.

condition is required to determine the spalling contour. Thus, arc B_3M in Figure 11(d) is drawn with a circle center at O_p and a radius of O_pB_3, where M is the intersection of arc B_3M and radius O_pD_1. Point N in Figure 11(e) is defined similarly as point M in Figure 10(d). Finally, the spalling contour is approximated based on arc B_3M or A_3N.

5.2. Type II Image. The geometric features in Figure 12(a) are defined as $l_i = 0$ and $L_i > 0$. Similar to Type IV image presented in Section 4.4, $l_i = 0$ implies that a small area around C_0 is intact, and $L_i > 0$ implies that damage is likely to occur entirely on one side of C_0.

Two feasible spalling contours are illustrated in Figures 12(c) and 12(d). Because only the coordinates of B_3 in Figure 12(c) are known, the additional point Q, the intersection of circular arc B_3Q, and line segment O_pO_s must be specified to determine the spalling contour. B_3Q is drawn with a circle center of O_p and a radius of OB_3. Similarly, point Q in Figure 12(d) is located at the intersection of line segment O_pO_s and circular arc A_3Q, drawn with a circle center of O_p and a radius of OA_3. Subsequently, arcs B_3Q and A_3Q for approximating the spalling contour can be determined.

6. 3-D Reconstruction of Defective Pile

Extracting information from multiple MSIS images obtained from uniformly distributed scan points in the vicinity of a pile is the basis of section reconstruction. The defect type is first predetermined based on the defect feature extracted from the MSIS image; subsequently, all feasible defect contours are ascertained using the methods described in Sections 3 and 4. However, for defects spanning multiple

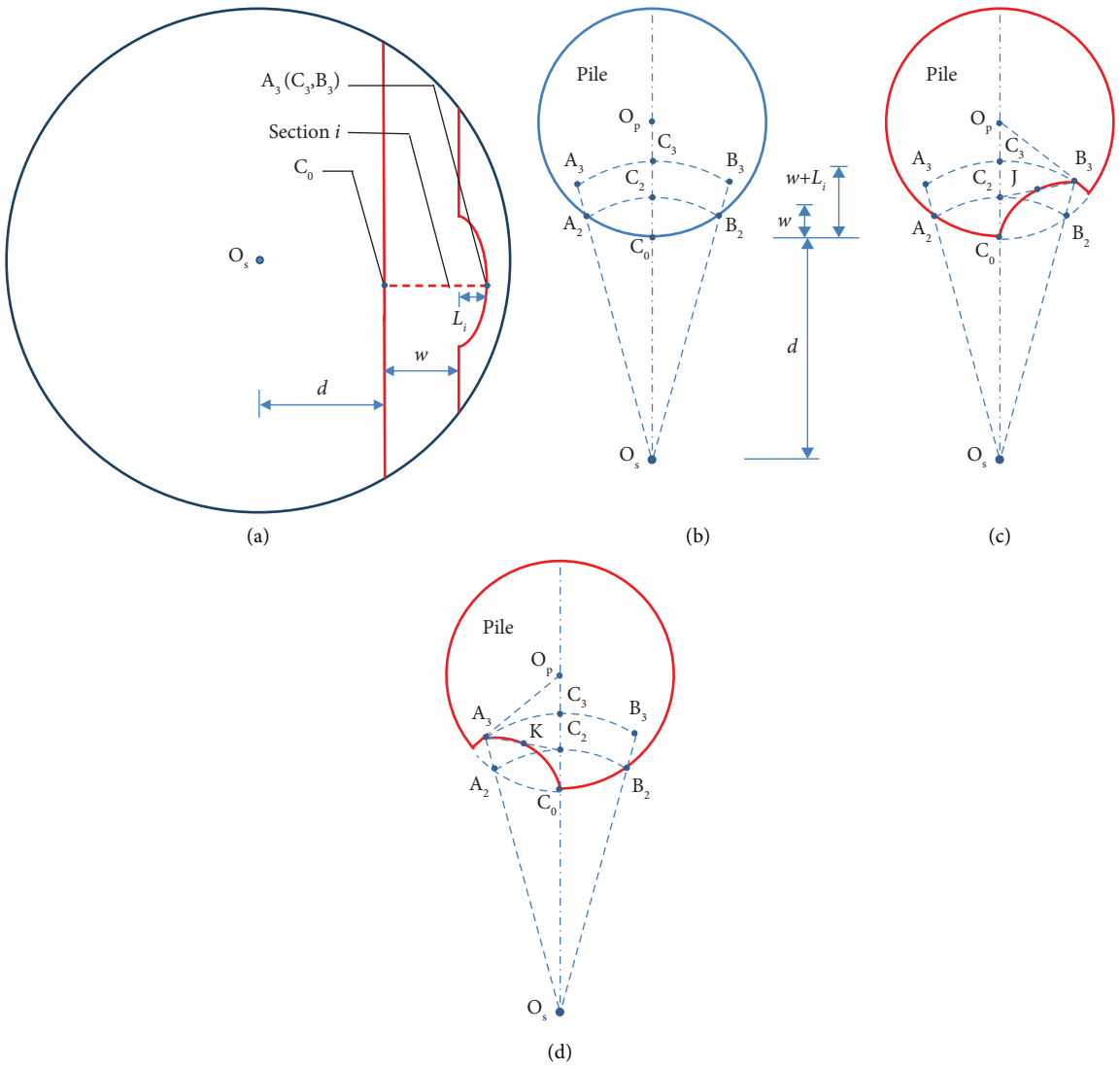

FIGURE 10: Two feasible cavity contours corresponding to Type IV image. (a) Type IV image. (b) Top view of Section *i*. (c) The 1st feasibility. (d) The 2nd feasibility.

scan fields, the necessary information must be extracted for reconstruction using multiple images.

6.1. Section Recognition. In a single-scan field reconstruction, most of the reconstructed defect contours are smooth arcs determined by two or three feature points with known coordinates. For a defect spanning multiple scan fields, its contour is expected to be continuous, and a smooth curve is reconstructed by connecting the feature points in the MSIS images. Moreover, the reconstructed curve must be consistent with the geometric features of each MSIS image.

An example of a large-cavity contour reconstruction is shown below. The images shown in Figures 9(a) and 10(a) are assumed to be known MSIS images obtained at adjacent scan points. First, as shown in Figure 13(a), all feature points are extracted from the two known images, and all feasible cavity contours are drawn. Subsequently, the most feasible cavity contour is assumed to be similar to the fusion of green arc AC and blue arc BD in Figure 13(b). Finally, the cavity contour shown in Figure 13(c) is regarded as a nonuniform rational B-spline connecting *A*, *B*, C, and *D* smoothly.

6.2. Rebuilding 3-D Model of a Defective Pile. As shown in Figure 14, the 3-D model of a defective pile was reconstructed by assembling all the recognized sections smoothly in AutoCAD. AutoCAD can be used to form the 3-D model, and the accuracy of the 3-D reconstructed model improves as the number of sections increases.

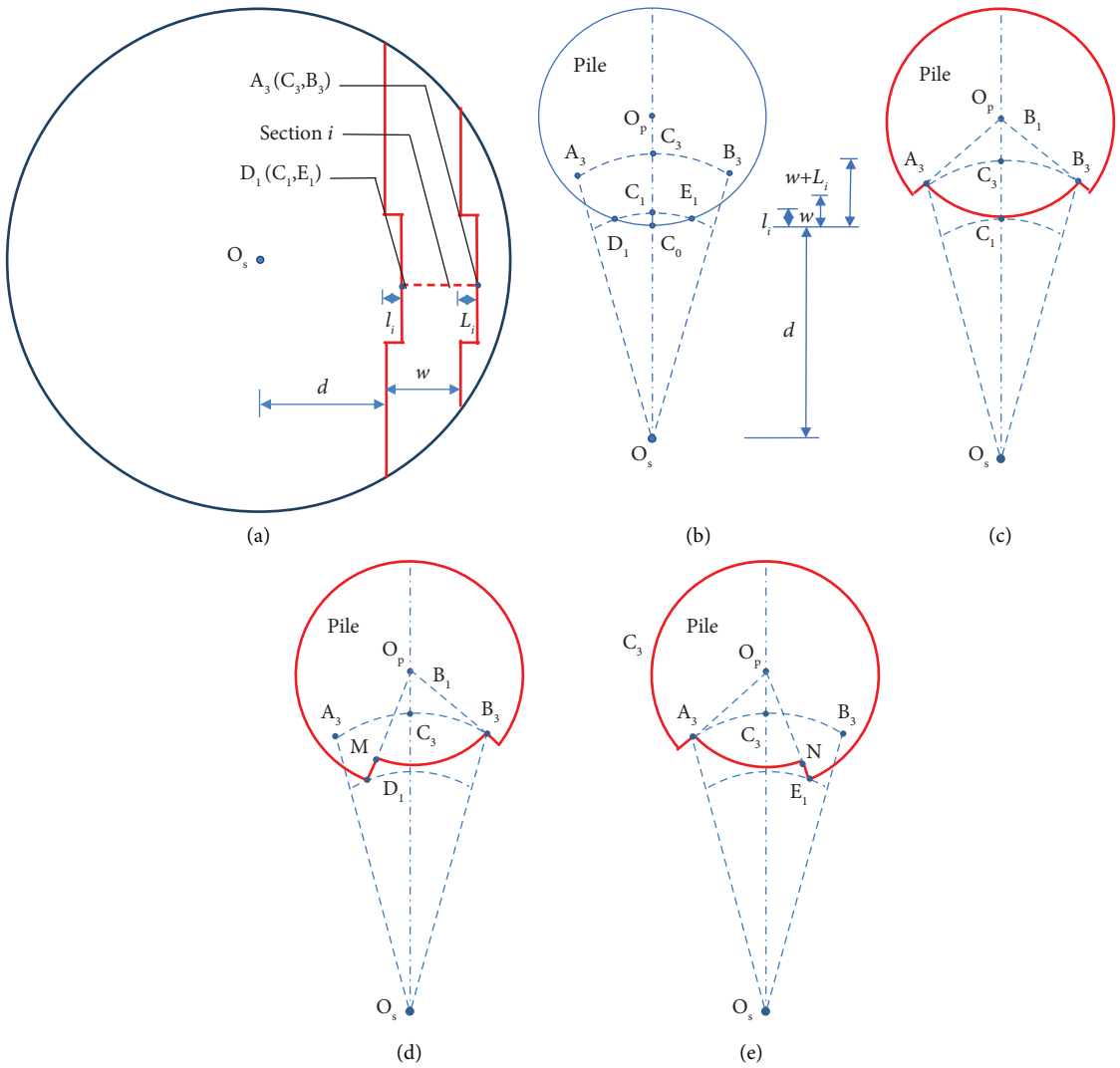

FIGURE 11: Three feasible spalling contours corresponding to Type I image. (a) Type I image. (b) Top view of Section *i*. (c) The 1st feasibility. (d) The 2nd feasibility. (e) The 3rd feasibility.

7. Procedure of the Entire Pile Reconstruction

Figure 15 illustrates the procedure of the entire 3-D reconstruction of an underwater defective pile. It contains (1) setting a certain number of measuring points evenly around the pile; (2) placing the sonar on the measuring points to acquire the successive sonar images of the pile from different positions; (3) applying some image processing methods, including denoising, edge enhancement, and histogram equalization to the raw MSIS images to obtain clear features; (4) identifying and locating the defect based on the different acoustic features in Figures 6(c)–6(e); (5) dividing the area of defect in the MSIS image into several sections in the vertical direction; (6) applying the proposed method in Sections 4 and 5 to determine the cavity and spalling contour in each section; (7) applying the proposed method in Section 6.1 to obtain the defect contour in section in case that the defect spans two successive images; and (8) rebuilding the 3-D model of a defective pile by assembling all the recognized sections smoothly in AutoCAD.

8. Experimental Verification for Proposed 3-D Pile Reconstruction

In this experiment, only nine MSIS images were obtained at nine scan points around a reduced-scale concrete pile. Subsequently, 20 cross-section contours of the pile were recognized based on the feature points extracted from the MSIS images. Finally, a 3-D pile model was developed based on the recognized 20 contours. A comparison between the 3-D model and actual concrete pile demonstrated the applicability of the proposed reconstruction method.

8.1. Test Setup. The reduced-scale pile was constructed using a concrete column measuring 1140 and 1300 mm in diameter and height, respectively. Considering the appearance of multiple defects, two defect combinations, i.e., "spalling + small cavities + exposed steel bars (defect combination I)" and "large cavities + exposed steel bars (defect combination II)," were generated on the column surface. Cavities

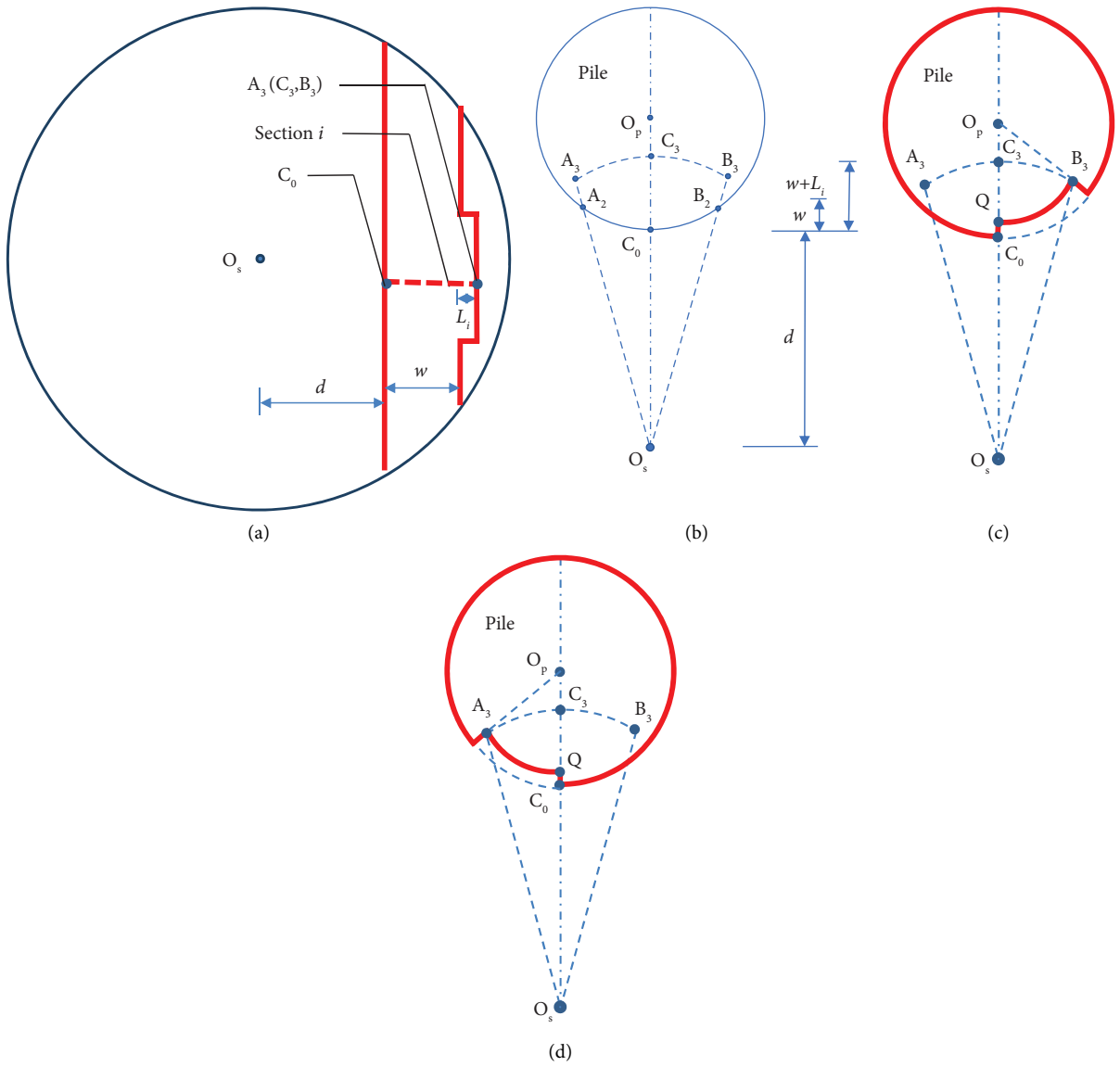

FIGURE 12: Two feasible spalling contours corresponding to Type II image. (a) Type II image (b) Top view of Section *i*. (c) The 1st feasibility. (d) The 2nd feasibility.

1–5 and 1*–5*, as shown in Figures 16(a)–16(d), were similar in size; however, the former exhibited a smooth surface, whereas the latter exhibited a rough surface. The diameters of the exposed vertical bars and stirrups were 16 and 8 mm, respectively. Figure 16(e) shows a top view of nine scan points denoted as P_0–P_8, which were distributed uniformly around the column. Details regarding the defects exposed in the scan fields of P_0–P_8 are shown in Figure 16(e). In Figures 16(c) and 16(d), 20 cross sections (*S*0 to *S*19) distributed evenly from the bottom of the pool to the water surface with a vertical spacing of approximately 6 cm are represented by the dotted green lines. Table 1 lists the defect sizes in detail.

The test was conducted in a concrete pool measuring approximately 7.5 m (length) × 5.5 m (width) × 1.5 m (depth) (see Figure 16(f)). In contrast to practical scanning, the MSIS and column were fixed at two preconfigured points in the water pool at a distance of 750 mm. The column was rotated using a steel support placed under the column. A plastic protractor was attached on the top surface of the column to measure the column rotation and ensure that the MSIS aimed at the scan point accurately at each scan. The MSIS used in this test was an MS1000 produced by Kongsberg Co. Ltd., Norway. In the experiment, the transmitting frequency, the aperture angle in the horizontal direction, the imaging distance, the scan speed, and the scan mode of MS1000 were set to 1.2 MHz, 28°, 5 m, 18 s/360°, and 0.225° per step, respectively.

Furthermore, the test was conducted based on the requirement that the subsequent reconstruction can only be performed based on the analyses of the obtained MSIS images. Information regarding the sizes and positions of the defects on the column surface was unknown prior to the scan.

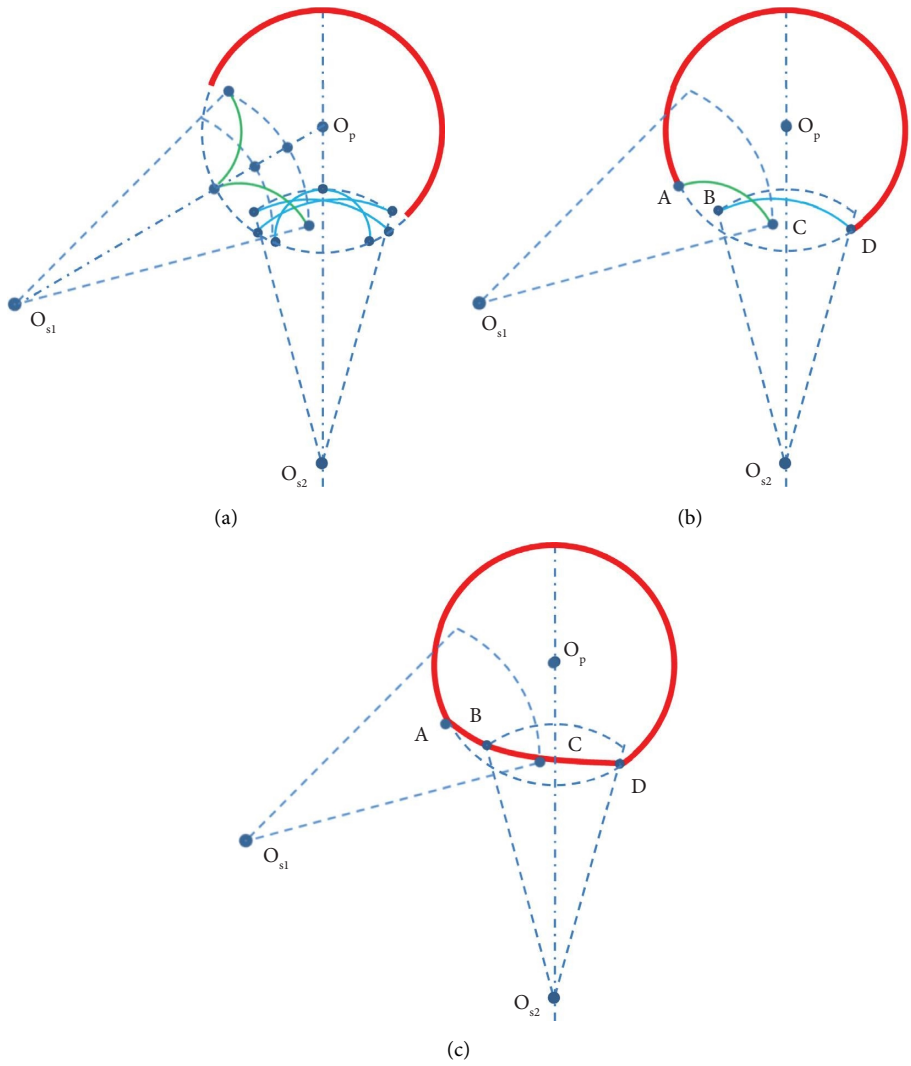

FIGURE 13: Cavity contour recognized by two successive MSIS images. (a) All feature points and contours. (b) Two feasible contours. (c) The final recognized cavity contour.

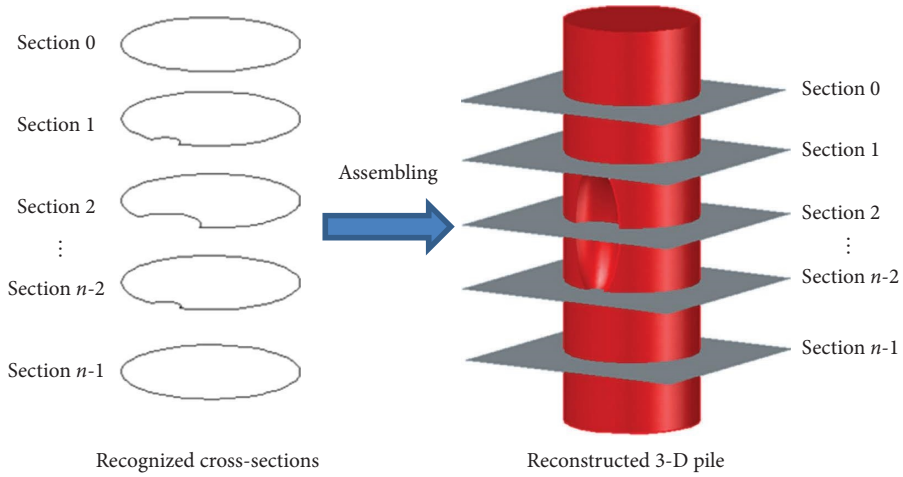

FIGURE 14: The 3-D model reconstruction based on the recognized sections.

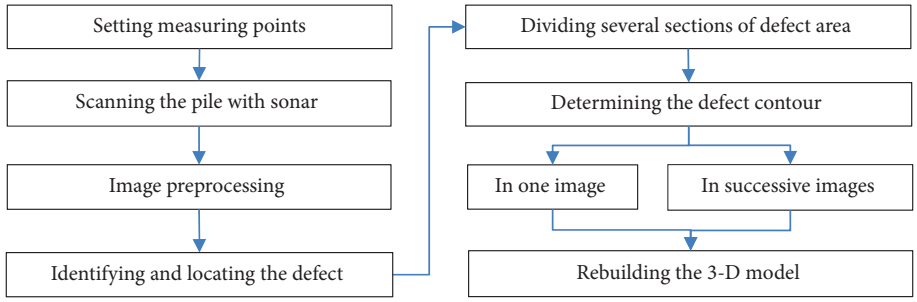

Figure 15: Procedure of the entire pile reconstruction.

8.2. 3-D Reconstruction of the Column. Figures 17(a)–17(i) show nine MSIS images obtained from P_0 to P_8 and the measurements necessary for contour reconstruction. All images were preprocessed meticulously. As an example, the recognition process for $S5$ is described in detail in the following. A comparison between the recognized contour (in blue) and the actual contour (in violet) is presented in Figures 18(a)–18(j). The pile surface that has not been identified (named contour to be recognized) is indicated in orange. The recognized contour indicates that the boundary of the region has been determined by the proposed method. The contour to be recognized represents the boundary that has not been identified. Thus, it is assumed to be an intact arc.

Figure 17(a) shows that no damage occurred to the pile surface within the scan field. In Figure 17(b), the approximate linear outer contour of the yellow stripe indicates that damage occurred entirely on one side of line P_1O within the scan field in Figure 16(e), and the convex inner contour of the bright stripe indicates that a cavity might occur. Because the geometric features of Figure 17(b) are consistent with those of the case analyzed in Section 4.4, the coordinates of feature points A_1 and B_1 and additional point D_1 in the polar coordinate system and the recognized contour of the partial cavity were determined based on the measured horizontal distances among P_1, A_1, and B_1, as shown in Figure 18(a). The subscript "1" implies that the points are within the scan field of P_1. Moreover, spalling within the scan field is unrecognizable in this stage owing to its ambiguous features.

The MSIS image obtained at P_2, as presented in Figure 17(c), shows linear concavities and convexities on the outer and inner contours of the yellow stripe. These features signify that spalling and cavity were present in the same scan range. However, ascertaining whether the cavity is located on the left or right side of line P_2O in Figure 16(e) is challenging owing to insufficient information extracted from Figure 17(c). Thus, by referring to Figures 18(b) and 18(c), one can observe that the cavity was located on the left and right sides of P_2O, respectively.

The contour recognitions shown in Figures 17(d) and 17(e) are based on the cases in Sections 4.4 and 5.1, respectively. Figure 17(e) shows that only spalling appeared within the scan field of the MSIS at P_4, which implies that the cavity in the scan field of the MSIS at P_3 must be on the right side of line P_3O (Figure 17(e)). Therefore, Figures 18(b) and 18(c) were revised to Figures 18(d) and 18(e), respectively, to update the recognized contour. However, distinguishing whether the recognized contours in Figure 18(d) or 18(e) are closer to the actual contour remains difficult. Thus, based on Presumption II in Section 3.3, the contour in Figure 18(e) was selected as its damage area (70, 538 mm^2) was larger than that of the other contour (60, 766 mm^2).

The features in Figure 17(f) imply that the extension of spalling was confined to within the scan field and did not exceed line P_5O. Figure 18(f) shows the updated defect contour, including feature points A_5 and B_5, whose coordinates were determined based on the Type II spalling image. Similarly, Figure 18(f) was further revised to Figure 18(g), and key points A_6 and B_6 as well as an additional point D_6 are shown.

The analysis of Figure 17(h) is similar to that of Figure 17(d). Owing to insufficient information for determining the side on which line P_7O was situated, we speculated that two contours were feasible, i.e., those shown in Figures 18(h) and 18(i). Figure 17(i) indicates that no defects existed in the sonar scan field at $P8$. Because the cavity defined by curve $A_7B_6B_7$ in Figure 18(h) entered the scan field of the MSIS at $P8$, this recognized contour was reasonably excluded, and the recognized contour shown in Figure 18(i) was accepted. The final recognized defect contour of $S5$ is shown in Figure 18(j), and the polar coordinates of all the recognized feature points and additional points on $S5$ are listed in Table 2.

Figures 19(a)–19(t) show the comparisons between the recognized contours (in blue) and the actual contours (in violet) of $S0$–$S19$. The actual and recognized damage areas of cavities 1–5, cavities 1^*–5^*, and spalling are presented in Tables 3 and 4. The errors between the two types of areas are listed in the tables.

Three conclusions were inferred from the comparison. First, the location and quantity of the recognized defects were consistent with those on the defective column, and the recognition accuracy increased with the cavity area in each section. Most errors between the recognized and actual damage areas of small cavities (cavities $1/1^*$ to $4/4^*$) exceeded 50%, whereas the corresponding error between the recognized and actual damage areas for cavity $5/5^*$ was less than 10%. Second, the areas of most recognized cavities exceeded those of the actual cavities owing to the "intentional" amplification of the contour recognition results. Third, the recognized spalling area was similar to the actual spalling area, where most errors were less than 10%. This

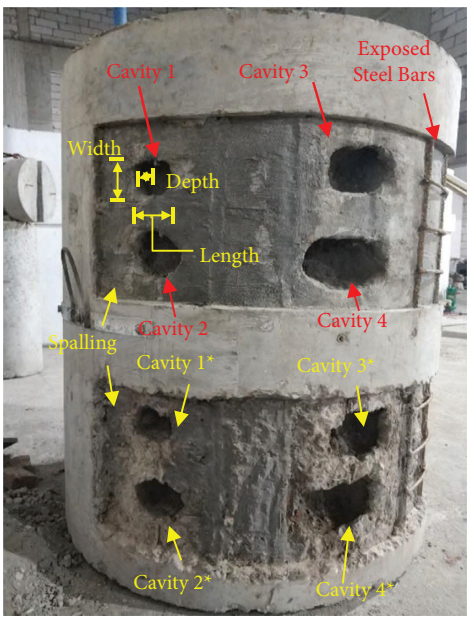

(a)

(b)

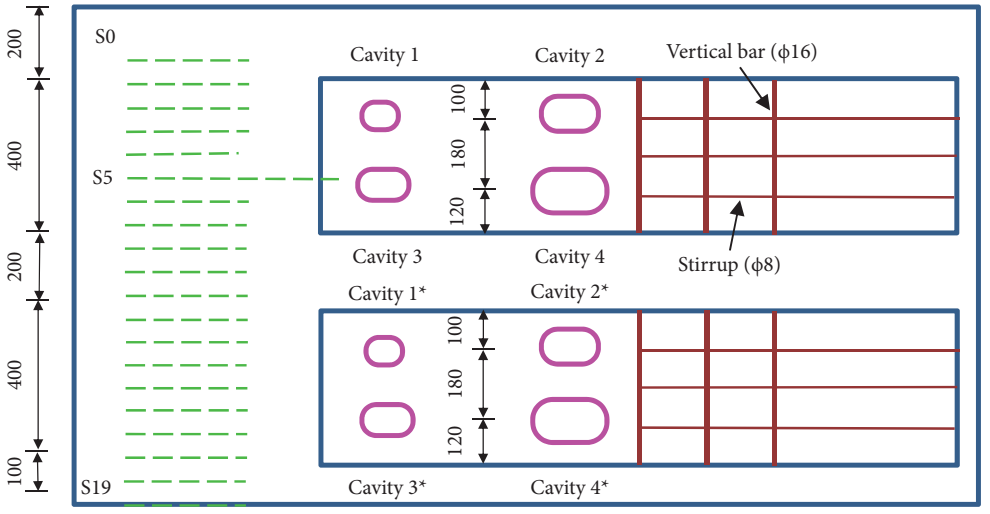

--- : Horizontal sections (S0-S19)

(c)

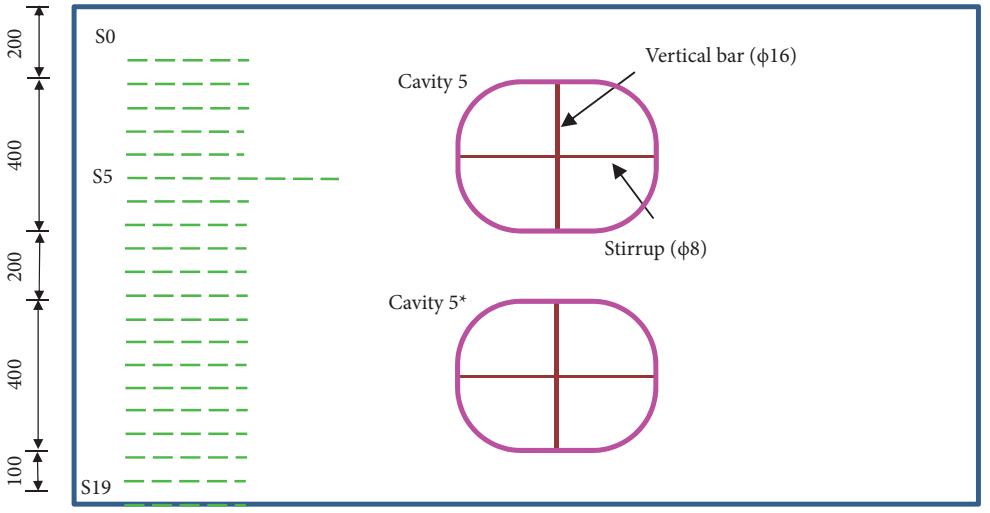

--- : Horizontal sections (S0-S19)

(d)

Figure 16: Continued.

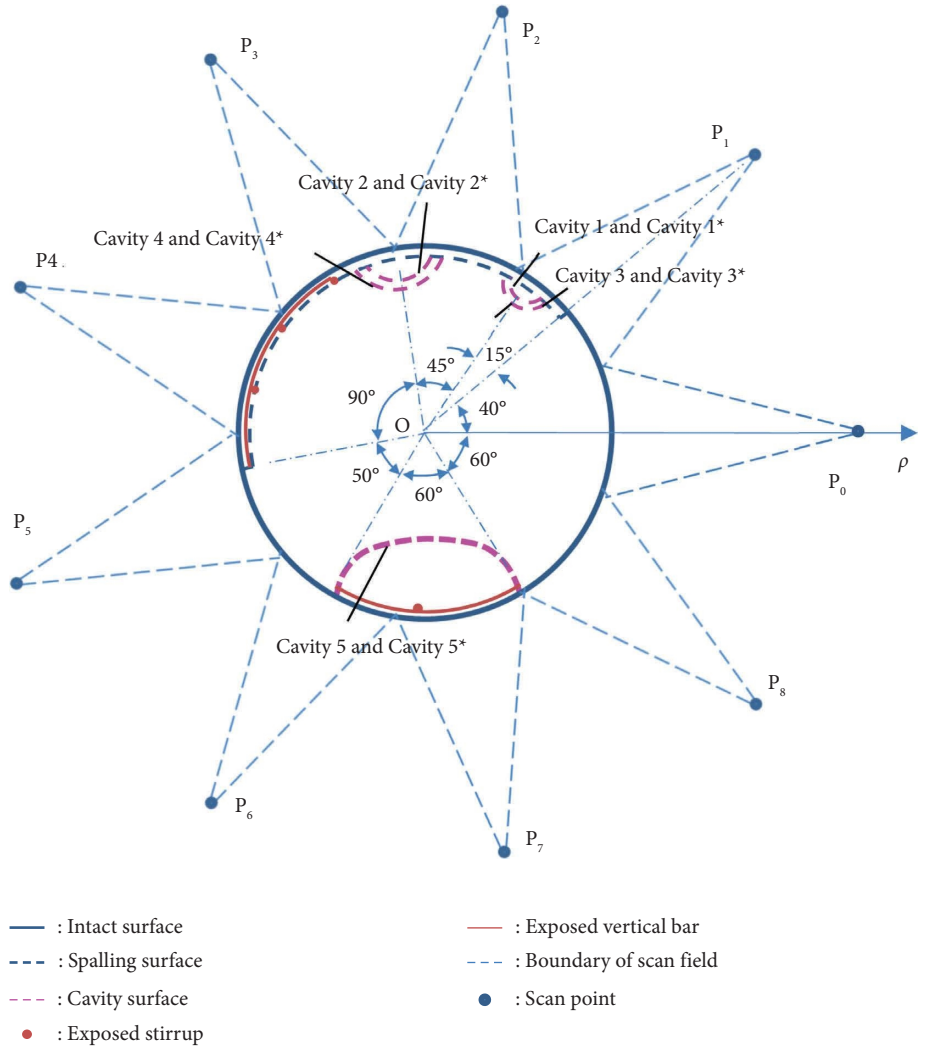

(e)

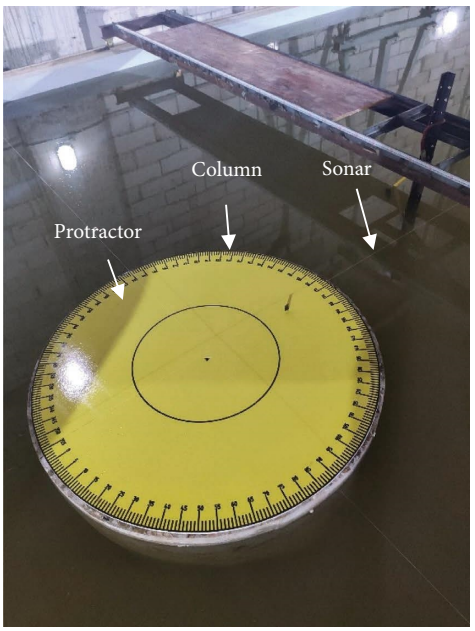

(f)

Figure 16: Defects placed on the column surface (unit: mm). (a) Defect combination I. (b) Defect combination II. (c) Details about defect combination I in the vertical direction. (d) Details about defect combination II in the vertical direction. (e) Details about defect combinations I and II in the horizontal direction. (f) The column and the sonar in the water pool.

Table 1: Maximum sizes of defect combination I (unit: mm).

	Depth	Width	Length
Spalling	30	400	1518
Cavity 1 and cavity 1*	60	80	80
Cavity 2 and cavity 2*	80	90	120
Cavity 3 and cavity 3*	100	100	160
Cavity 4 and cavity 4*	120	110	200
Cavity 5 and cavity 5*	250	400	608

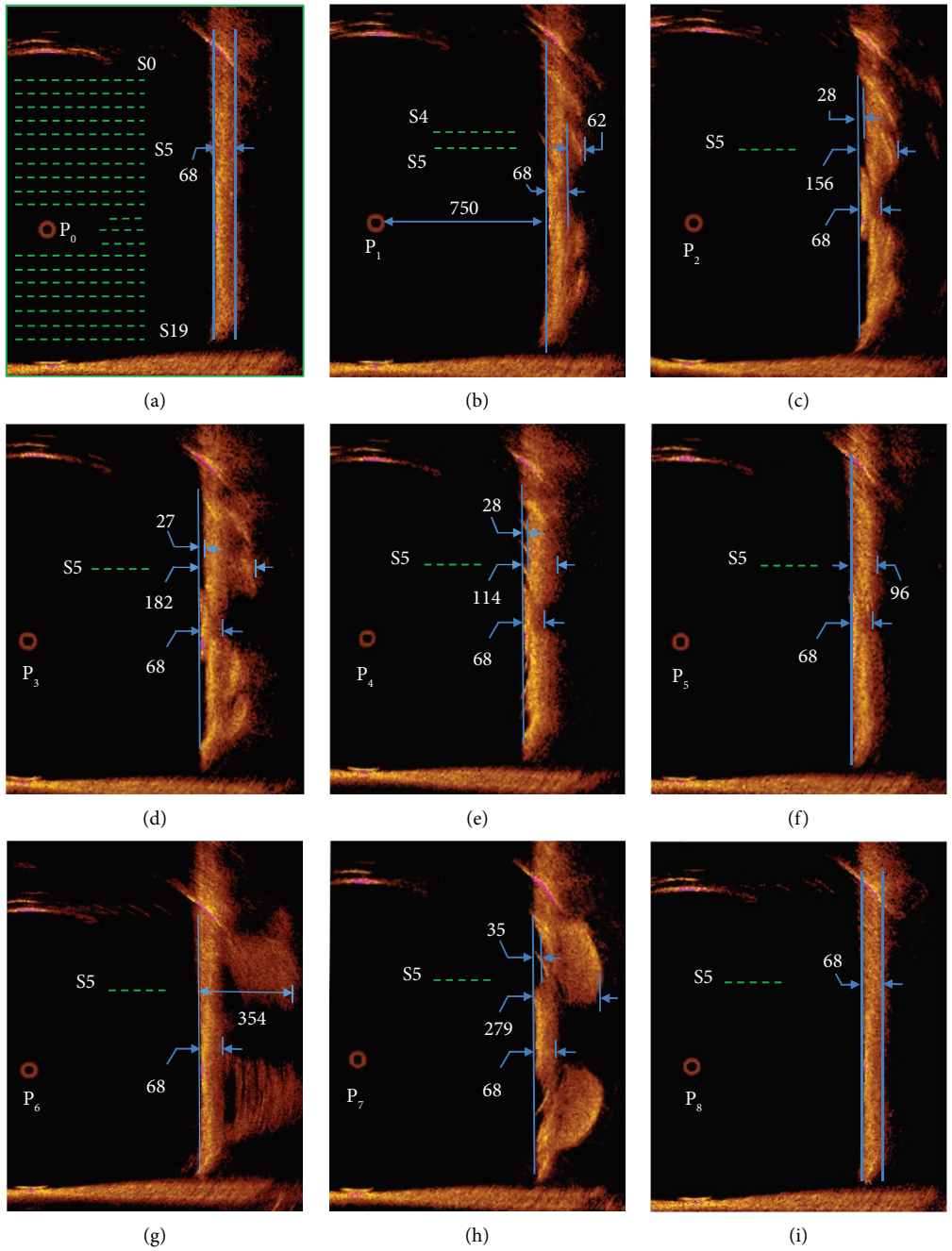

Figure 17: The obtained MSIS images of the defective column (unit: mm). (a) 0°, (b) 40°, (c) 80°, (d) 120°, (e) 160°, (f) 200°, (g) 240°, (h) 280°, and (i) 320°.

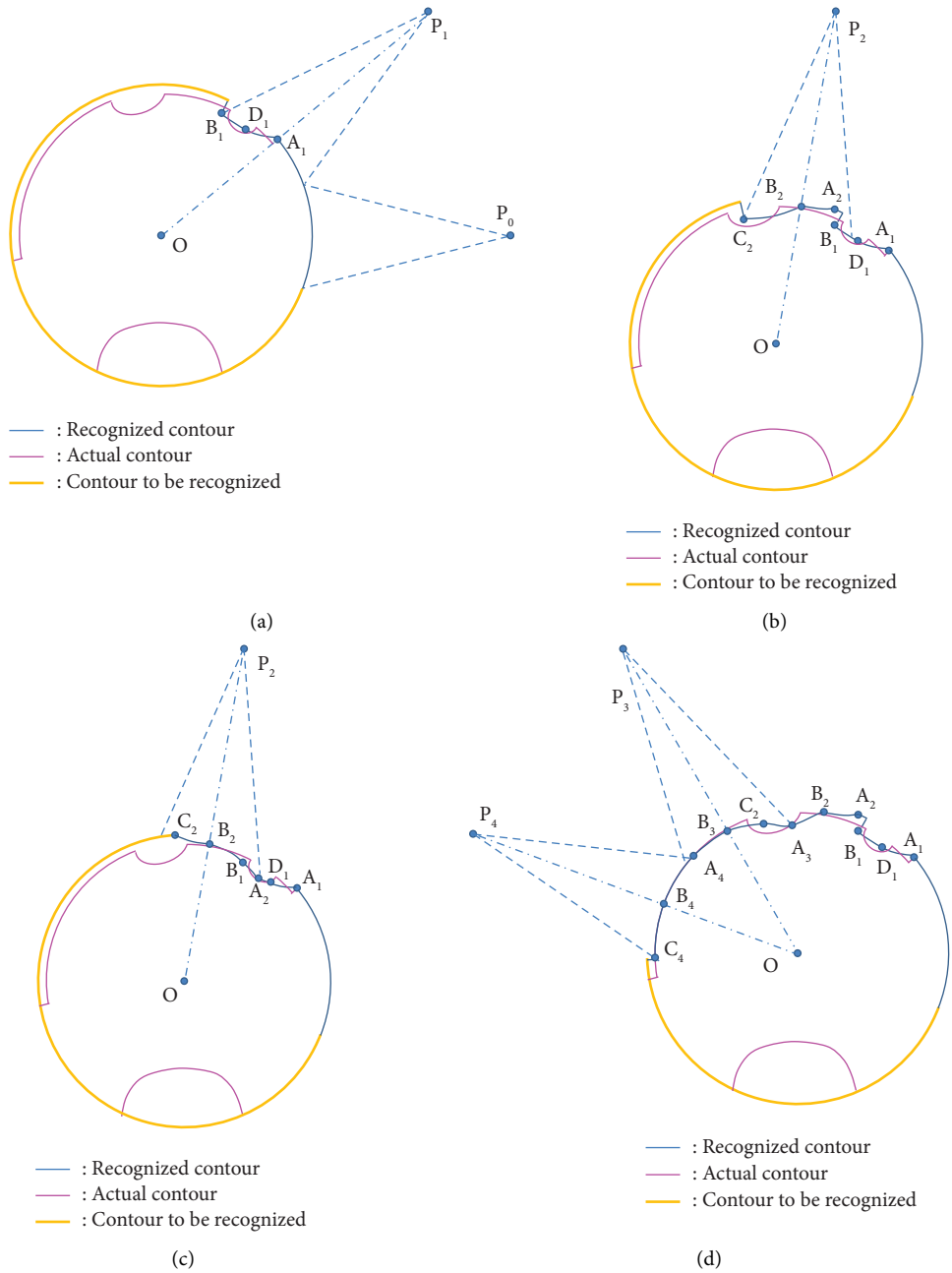

Figure 18: Continued.

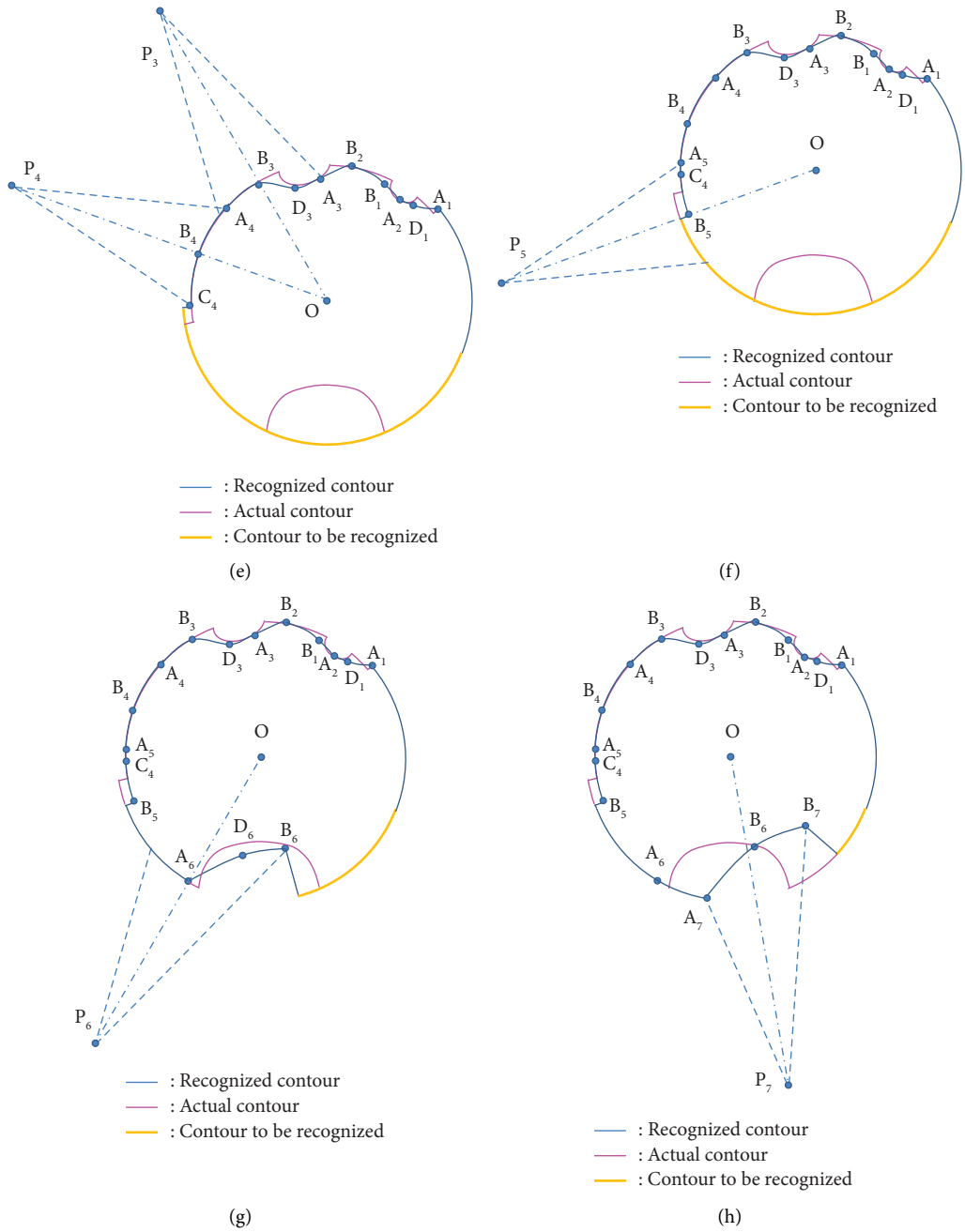

Figure 18: Continued.

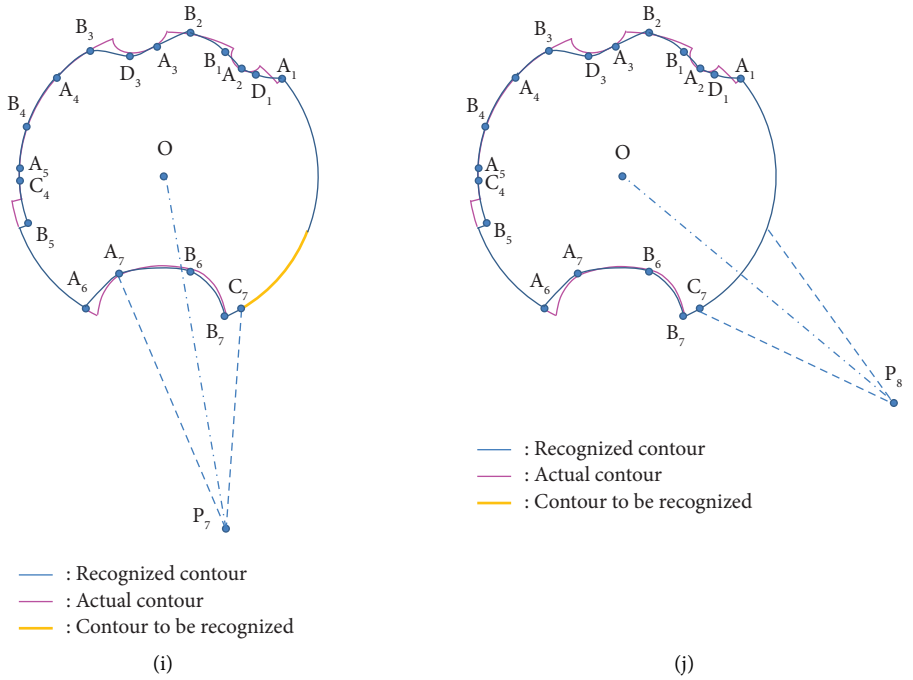

Figure 18: Recognizing process of defect contour. (a) Recognized contour from MSIS images (P_0 and P_1). (b) The 1st feasible contour recognized from the MSIS images (P_0 and P_2). (c) The 2nd feasible contour recognized from the MSIS images (P_0 and P_2). (d) The 1st feasible contour recognized from the MSIS images (P_0 and P_4). (e) The 2nd feasible contour recognized from the MSIS images (P_0 and P_4). (f) Recognized contour from the MSIS images (P_0 and P_5). (g) Recognized contour from the MSIS images (P_0 and P_6). (h) The 1st feasible contour recognized from the MSIS images (P_0 and P_7). (i) The 2nd feasible contour recognized from the MSIS images (P_0 and P_7). (j) The final recognized contour.

Table 2: The polar coordinates of the key points and the additional points (unit: mm).

Image number	Key point			Additional point
a	A_1 (570, 40°)	B_1 (519, 64.00°)		D_1 (503, 53.35°)
b	A_2 (570, 66.27°)	B_2 (544, 80.00°)	C_2 (499, 105.74°)	
c	A_2 (499, 54.26°)	B_2 (544, 80.00°)	C_2 (570, 93.73°)	
d	A_3 (481, 92.39°)	B_3 (544, 120.00°)		D_3 (503, 106.60°)
e	A_4 (538, 136.23°)	B_4 (544, 160.00°)	C_4 (538, 183.77°)	
f	A_5 (534, 177.15°)	B_5 (544, 200.00°)		D_6 (401, 258.76°)
g	A_6 (570, 240°)	B_6 (373, 311.86°)	C_6 (373, 311.86°)	
h	A_7 (570, 260.59°)	B_7 (413, 316.66°)		
i	A_7 (413, 243.34°)	B_7 (570, 299.41°)		

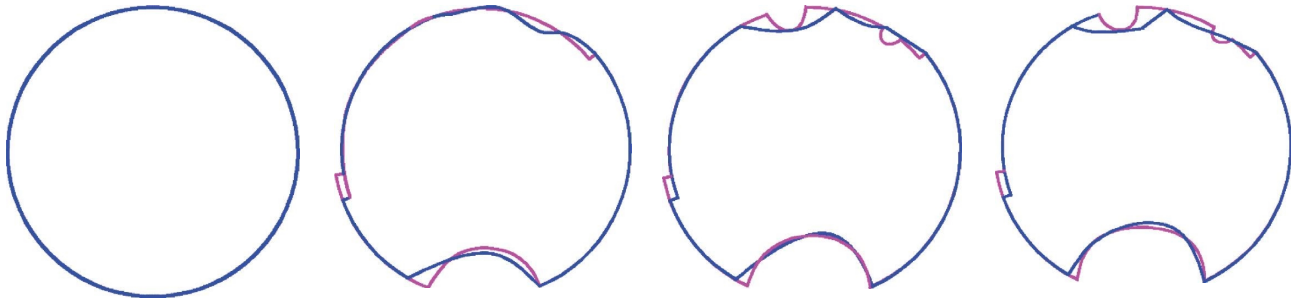

(a) (b) (c) (d)

Figure 19: Continued.

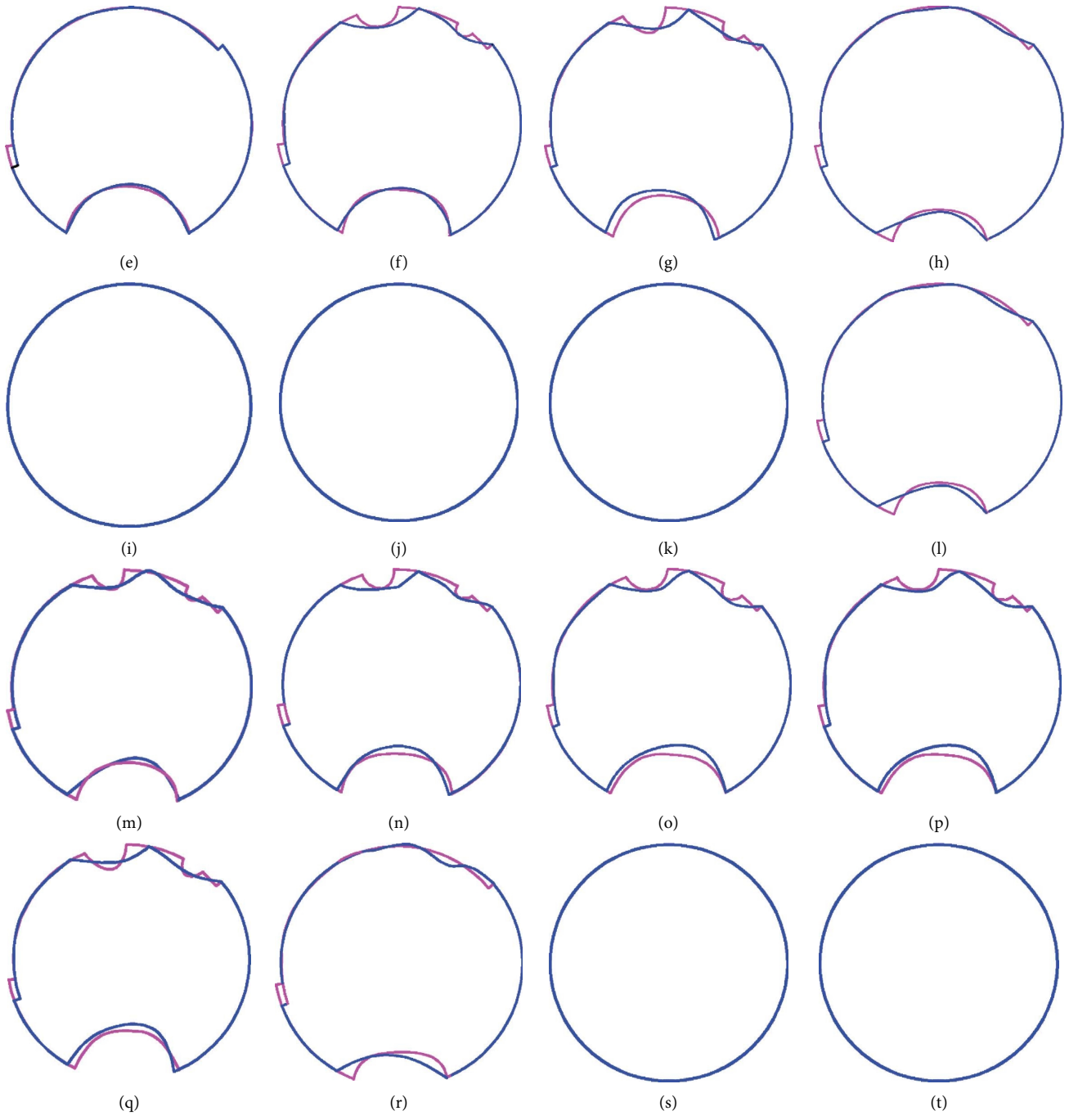

Figure 19: The recognized contours of $S0$–$S19$. (a) $S0$, (b) $S1$, (c) $S2$, (d) $S3$, (e) $S4$, (f) $S5$, (g) $S6$, (h) $S7$, (i) $S8$, (j) $S9$, (k) $S10$, (l) $S11$, (m) $S12$, (n) $S13$, (o) $S14$, (p) $S15$, (q) $S16$, (r) $S17$, (s) $S18$, and (t) $S19$.

indicates that the recognition of spalling in the actual scan is accurate because the spalling area in practical defective piles is large.

The reason for the remarkable errors in the recognized areas of cavities 1–4 and cavities 1^*–4^* is to simulate the real contours of the cavities with arcs. This approximation always tends to overestimate the cavity area. However, since these errors only exist in the case of a small cavity, they will not cause obvious errors in evaluating the safety of the defective piles.

Table 5 shows a comparison between the entire recognized defective areas and the actual defective areas on

Table 3: Real damage areas and recognized damage areas of cavities 1–4 and cavities 1*–4* (unit: 10^3 mm^2).

	Real	Recognized	Error
	Cavity 1		
*S*2	2.83	3.94	39.3%
*S*3	3.14	6.11	94.4%
*S*5	—	—	—
*S*6	—	—	—
	Cavity 2		
*S*2	—	—	—
*S*3	—	—	—
*S*5	5.92	9.90	67.2%
*S*6	6.16	11.05	79.3%
	Cavity 3		
*S*2	8.97	18.19	102.9%
*S*3	9.36	19.43	107.6%
*S*5	—	—	—
*S*6	—	—	—
	Cavity 4		
*S*2	—	—	—
*S*3	—	—	—
*S*5	12.05	22.06	83.0%
*S*6	12.85	21.54	67.7%
	Cavity 1*		
*S*12	2.83	4.12	46.0%
*S*13	3.14	5.93	88.7%
*S*15	—	—	—
*S*16	—	—	—
	Cavity 2*		
*S*12	—	—	—
*S*13	—	—	—
*S*15	5.92	9.95	68.1%
*S*16	6.16	12.19	98.0%
	Cavity 3*		
*S*12	8.97	17.83	98.7%
*S*13	9.36	19.99	113.6%
*S*15	—	—	—
*S*16	—	—	—
	Cavity 4*		
*S*12	—	—	—
*S*13	—	—	—
*S*15	12.05	23.25	92.9%
*S*16	12.85	20.96	63.2%

*S*1–*S*19. The recognized sections were similar to the actual sections, and the recognition error did not exceed 16%. Finally, as shown in Figure 20, a 3-D reconstructed model of the defective column was formed by connecting the 20 recognized sections smoothly. It is believed that the reconstruction errors will decrease further when the number of cross sections is increased and the distance between adjacent cross sections is reduced.

Table 4: Real damage areas and recognized damage areas of cavity 5, cavity 5*, and spalling (unit: 10^3 mm^2).

	Real	Rebuilt	Error	Real	Rebuilt	Error
		Cavity 5			*Spalling*	
*S*1	58.89	61.00	3.6%	43.59	47.43	8.8%
*S*2	84.79	87.07	2.7%	43.59	47.91	9.9%
*S*3	100.30	104.54	4.2%	43.59	46.68	7.1%
*S*4	120.33	125.63	4.4%	43.59	49.91	14.5%
*S*5	102.47	108.64	6.0%	43.59	48.22	10.6%
*S*6	85.83	89.69	4.5%	43.59	47.35	8.6%
*S*7	60.13	57.35	4.6%	43.59	48.16	10.5%
		Cavity 5*				
*S*11	58.21	60.39	3.7%	43.59	47.27	8.4%
*S*12	84.03	88.25	5.0%	43.59	47.86	9.8%
*S*13	99.79	108.46	2.7%	43.59	46.87	7.5%
*S*14	120.12	127.33	6.0%	43.59	48.56	11.4%
*S*15	101.64	106.60	4.9%	43.59	48.63	11.5%
*S*16	85.33	89.46	4.8%	43.59	46.58	6.8%
*S*17	59.48	61.54	3.9%	43.59	47.58	9.1%

Table 5: Errors between the recognized defective areas and the real defective areas (unit: 10^3 mm^2).

	The real defective area	The rebuilt defective area	Error (%)
*S*0	0	0	0
*S*1	102.48	108.43	5.8
*S*2	140.18	157.11	12.1
*S*3	156.39	176.76	13.0
*S*4	163.92	175.54	7.1
*S*5	164.03	188.82	15.1
*S*6	152.19	169.63	11.5
*S*7	103.72	111.38	7.4
*S*8	0	0	0
*S*9	0	0	0
*S*10	0	0	0
*S*11	101.80	107.66	5.8
*S*12	139.01	158.06	13.7
*S*13	155.88	174.34	10.2
*S*14	163.71	175.89	11.8
*S*15	163.54	188.43	15.2
*S*16	147.80	169.19	14.5
*S*17	103.07	109.36	6.1
*S*18	0	0	0
*S*19	0	0	0

Additionally, some exposed stirrups were scanned, as shown in Figures 17(e) and 17(h) however, the trace of the exposed vertical bars was ambiguous. In future studies, we shall focus on identifying exposed steel bars accurately. Based on the design drawing, a distinguished feature of exposed reinforcement is that the maximum depth of the defect in the rebuilt section exceeds the thickness of the concrete cover.

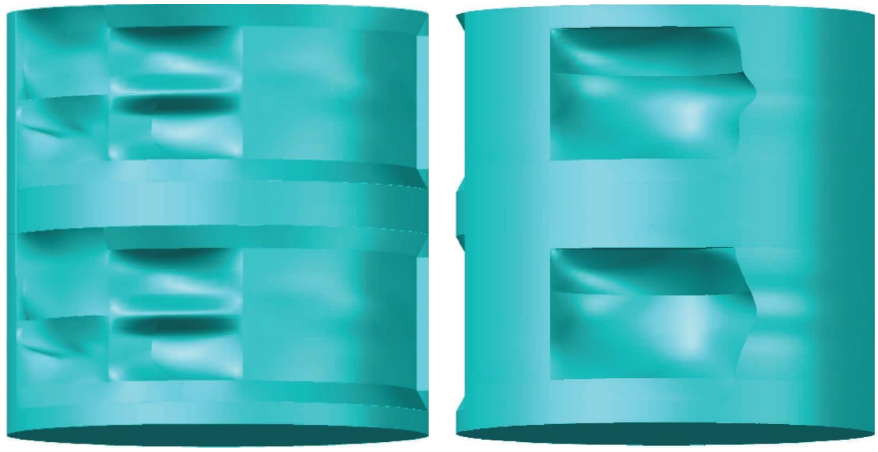

(a) (b)

Figure 20: The 3-D reconstructed model of the defective column. (a) Defect combination I. (b) Defect combination II.

9. Conclusions

Herein, a rapid 3-D model reconstruction method for cavity and spalling on an underwater defective pile based on a few 2-D images obtained using an MSIS was presented. The primary contributions of this study are as follows:

(1) Although the relative positions between the MSIS and defect were unknown prior to scanning the underwater, all possible relative positions during cavity and spalling contour recognition can be summarized into four and two types, respectively. A one-to-one correspondence between the geometric features of the MSIS image and the actual defect in each possibility was established to rapidly determine some feature points and defect contours. The proposed method required the coordinates of a few feature points from MSIS images to avoid the typical inefficiency of 3-D modeling, which necessitated the extraction of numerous feature points from numerous sonar images.

(2) During defect contour recognition, the number of feasible recognized contours should be minimized. By synthesizing the information extracted from adjacent images encompassing the defect area, some infeasible contour candidates can be excluded, which is otherwise not realizable if only information from one image is available.

(3) The results from the 3-D model reconstruction of a reduced-scale defective pile showed that the maximum recognition error of the rebuilt defective area did not exceed 16%, which verified the applicability of the proposed method for practical MSIS scanning and 3-D model reconstruction.

The limitations of the proposed method were as follows. First, because existing MSIS-carrying platforms, such as survey vessels and autonomous underwater vehicles, cannot remain adequately stable in flowing water, the proposed method is applicable to cases involving calm water. Second, the target of the proposed method is a monopile. In practice, the pile cap and adjacent piles may obstruct the scan field at certain scan points at the vicinity of a single pile. Third, some defects, such as concrete cracks and scours, were not included in the objects reconstructed using the proposed method.

This study provides a basis for obtaining the solutions to these problems in the future. A customized platform that can anchor the sonar firmly in flowing water as well as shift and assemble it easily around a pile-cap foundation should be designed and manufactured. Additionally, the positions of points for scanning the MSIS should be optimized to ensure that the scanning region encompasses the entire surface of the defective pile and avoids the obstruction of the cap and adjacent piles.

Data Availability

The data used to support the findings of this study are available from the corresponding author upon reasonable request.

Conflicts of Interest

The authors declare that they have no conflicts of interest.

Acknowledgments

This study was financially supported by the Guiding Key Project for the Social Development of Fujian Province, China (no. 2020Y0015), the Key Project of Fujian Natural Science Foundation (no. 2022J02016), and the Transportation and Communication Science and Technology Project of Fujian Province (no. 201716). The authors also express their gratitude to Editage (https://www.editage.cn/) for English language editing.

References

[1] H. H. Chen, W. N. Chuang, and C. C. Wang, "Vision-based line detection for underwater inspection of breakwater

construction using an ROV," *Ocean Engineering*, vol. 109, pp. 20–33, 2015.

[2] H. M. La, N. G. Gucunski, S.-H. Kee, and L. Nguyen, "Visual and acoustic data analysis for the bridge deck inspection robotic system," in *Proceedings of the 31st International Symposium on Automation and Robotics in Construction and Mining (ISARC 2014)*, Sydney, Australia, July 2014, https://pdfs.semanticscholar.org/b3bd/feca92f5fb44b5233f5f30127147552bde10.pdf.

[3] P. Shi, X. Fan, J. Ni, and G. A. Wang, "A detection and classification approach for underwater dam cracks," *Structural Health Monitoring*, vol. 15, no. 5, pp. 541–554, 2016.

[4] F. R. Dalgleish, F. M. Caimi, W. B. Britton, and C. F. Andren, "Improved LLS imaging performance in scattering-dominant waters," *Ocean Sensing and Monitoring*, vol. 7317, Society of Photographic Instrumentation Engineers, Cergy-Pontoise, France, 2009.

[5] S. Negahdaripour and A. Sarafraz, "Improved stereo matching in scattering media by incorporating a backscatter cue," *IEEE Transactions on Image Processing*, vol. 23, no. 12, pp. 5743–5755, 2014.

[6] Y. Schechner and N. Karpel, "Recovery of underwater visibility and structure by polarization analysis," *IEEE Journal of Oceanic Engineering*, vol. 30, no. 3, pp. 570–587, 2005.

[7] P. Shi, X. Fan, J. Ni, Z. Khan, and M. Li, "A novel underwater dam crack detection and classification approach based on sonar images," *PLoS One*, vol. 12, no. 6, Article ID e0179627, 2017.

[8] R. R. Murphy, E. Steimle, M. Hall et al., "Robot-assisted bridge inspection," *Journal of Intelligent and Robotic Systems*, vol. 64, no. 1, pp. 77–95, 2011.

[9] Ł. Topczewski, J. Cieśla, P. Mikołajewski, P. Adamski, and Z. Markowski, "Monitoring of scour around bridge piers and abutments," *Transportation Research Procedia*, vol. 14, pp. 3963–3971, 2016.

[10] S. Clubley, C. Manes, and D. Richards, "High-resolution sonars set to revolutionise bridge scour inspections," *Proceedings of the Institution of Civil Engineers - Civil Engineering*, vol. 168, no. 1, pp. 35–42, 2015.

[11] J. C. Fadool, G. Francis, and J. E. Clark, "Robotic device for 3D imaging of scour around bridge piles," in *Proceedings of the 36th Mechanisms and Robotics Conference*, New York, NY, USA, September 2013.

[12] D. Stromberg, "New Advances in Underwater Inspection Technologies for Railway Bridges over Water," *Railway Track and Structures*, vol. 107, no. 3, 2011.

[13] X. Zhang, Q. Li, Y. Ma, and Y. Jia, "Dimensional imaging sonar damage identification Technology research on sea-crossing bridge main pier pile foundations," in *Proceedings of the 2016 5th International Conference on Energy and Environmental Protection (ICEEP 2016)*, pp. 17-18, Shenzhen, China, September 2016.

[14] T. Ji, P. Li, W. Hu, and Y. Dai, "Indoor experimental study on influence of different underwater characteristics on 3D imaging sonar," *Port and Waterway Engineering*, vol. 554, no. 4, pp. 159–163, 2019.

[15] A. Rogers, C. Manes, and T. Tsuzaki, "Measuring the geometry of a developing scour hole in clear-water conditions using underwater sonar scanning," *International Journal of Sediment Research*, vol. 35, no. 1, pp. 105–114, 2020.

[16] A. Bolhasan, A. A. Hashim B, R. L. Wood, and B. Abualshar, "Data-Driven Prioritization and Empirical Predictions for Bridge Scour in Nebraska," 2022, https://rosap.ntl.bts.gov/view/dot/63534.

[17] S. Chaudhuri and K. Debnath, "Observations on initiation of pier scour and equilibrium scour hole profiles in cohesive sediments," *ISH Journal of Hydraulic Engineering*, vol. 19, no. 1, pp. 27–37, 2013.

[18] E. Westman and M. Kaess, "Wide Aperture Imaging Sonar Reconstruction Using Generative Models," in *Proceedings of the 2019 IEEE/RSJ International Conference on Intelligent Robots and Systems (IROS)*, pp. 3–8, Article ID 19299257, Macau, China, November 2019.

[19] J. McConnell, J. D. Martin, and B. Englot, "Fusing concurrent orthogonal wide-aperture sonar images for dense underwater 3D reconstruction," in *Proceedings of the 2020 IEEE/RSJ International Conference on Intelligent Robots and Systems (IROS)*, Las Vegas, NV, USA, October 2020.

[20] T. Zhang, S. Liu, X. He, H. Huang, and K. Hao, "Underwater target tracking using forward-looking sonar for autonomous underwater vehicles," *Sensors*, vol. 20, no. 1, p. 102, 2019.

[21] X. Fan, L. Lu, P. Shi, and X. Zhang, "A novel sonar target detection and classification algorithm," *Multimedia Tools and Applications*, vol. 81, no. 7, pp. 10091–10106, 2022.

[22] H. Zhang, M. Tian, G. Shao, J. Cheng, and J. Liu, "Target detection of forward-looking sonar image based on improved YOLOv5," *IEEE Access*, vol. 10, no. 2022, pp. 18023–18034, 2022.

[23] W. Kazimierski and G. Zaniewicz, "Determination of process noise for underwater target tracking with forward looking sonar," *Remote Sensing*, vol. 13, no. 5, p. 1014, 2021.

[24] N. Wawrzyniak and A. Stateczny, "MSIS image postioning in port areas with the aid of comparative navigation methods," *Polish Maritime Research*, vol. 24, no. 1, pp. 32–41, 2017.

[25] C. A. Mueller, T. Fromm, and H. Buelow, "Robotic Bridge Inspection within Strategic Flood Evacuation Planning," in *Proceedings of the 2017 Oceans*, pp. 19–22, Article ID 17303456, Aberdeen, UK, June 2017.

[26] J. E. DeVault, "Robotic system for underwater inspection of bridge piers," *IEEE Instrumentation and Measurement Magazine*, vol. 3, no. 3, pp. 32–37, 2000.

[27] E. Coiras, Y. Petillot, and D. M. Lane, "Multiresolution 3-D reconstruction from side-scan sonar images," *IEEE Transactions on Image Processing*, vol. 16, no. 2, pp. 382–390, 2007.

[28] J. Wang, J. Han, and P. Du, "Three-dimensional Reconstruction of underwater objects from side-scan sonar images," in *Proceedings of the Oceans 2017*, Aberdeen, UK, June 2017.

[29] B. Zerr and B. Stage, "Three-dimensional reconstruction of underwater objects from a sequence of sonar images, International Conference on Image Processing," *Proceedings*, vol. 3, pp. 927–930, 1996.

[30] T. M. Marston and J. L. Kennedy, "Volumetric acoustic imaging via circular multipass aperture synthesis," *IEEE Journal of Oceanic Engineering*, vol. 41, no. 4, pp. 852–867, 2016.

[31] T. Guerneve, K. Subr, and Y. Petillot, "Three-dimensional reconstruction of underwater objects using wide-aperture imaging SONAR," *Journal of Field Robotics*, vol. 35, no. 6, pp. 890–905, 2018.

[32] M. D. Aykin and S. Negahdaripour, "On 3-d Target Reconstruction from Multiple 2-d Forward-Scan Sonar Views," in *Proceedings of the IEEE Oceans Genova*, Genova, Italy, May 2015.

[33] K. Kim, N. Neretti, and N. Intratoir, "Mosaicing of acoustic camera images, radar, sonar and navigation," *IEEE Proceedings*, vol. 152, no. 4, pp. 263–270, 2005.

[34] N. Hurtos, "Fourier-based Registrations for Two-Dimensional Forward-Looking Sonar Image Mosaicing," in *Proceedings of the 2012 IEEE/RSJ International Conference on Intelligent Robots and Systems*, pp. 5298–5305, Vilamoura, Algarve, Portugal, October 2012.

[35] China Communications, *Ministry of Transport of the People's Republic of China, Standard for Technical Condition Evaluation of Highway Bridges*, China Communications Press, Beijing, China, 2011.

[36] Fujian Expressway, "Inspection report of underwater foundation of Shizitou bridge in ningshang expressway," 2016, https://www.emis.com/php/company-profile/CN/Fujian_Expressway_Development_CoLtd__%E7%A6%8F%E5%BB%BA%E5%8F%91%E5%B1%95%E9%AB%98%E9%80%9F%E5%85%AC%E8%B7%AF%E8%82%A1%E4%BB%BD%E6%9C%89%E9%99%90%E5%85%AC%E5%8F%B8__en_1738360.html.